Journal of Computational Physics **156,** 12–42 (1999)
Article ID jcph.1999.6350, available online at http://www.idealibrary.com on IDEAL®

ASPEN: A Fully Kinetic, Reduced-Description Particle-in-Cell Model for Simulating Parametric Instabilities[1]

H. X. Vu,* B. Bezzerides,* and D. F. DuBois†

*Applied Theoretical and Computational Division, Los Alamos National Laboratory, Los Alamos, New Mexico 87545; and †Theory Division, Los Alamos National Laboratory, Los Alamos, New Mexico 87545

Received March 18, 1999; revised August 11, 1999

A fully kinetic, reduced-description particle-in-cell (RPIC) model is presented in which deviations from quasineutrality, electron and ion kinetic effects, and nonlinear interactions between low-frequency and high-frequency parametric instabilities are modeled correctly. The model is based on a reduced description where the electromagnetic field is represented by three separate temporal envelopes in order to model parametric instabilities with low-frequency and high-frequency daughter waves. Because temporal envelope approximations are invoked, the simulation can be performed on the electron time scale instead of the time scale of the light waves. The electrons and ions are represented by discrete finite-size particles, permitting electron and ion kinetic effects to be modeled properly. The Poisson equation is utilized to ensure that space-charge effects are included. The RPIC model is fully three dimensional and has been implemented in two dimensions on the Accelerated Strategic Computing Initiative (ASCI) parallel computer at Los Alamos National Laboratory, and the resulting simulation code has been named ASPEN. We believe this code is the first particle-in-cell code capable of simulating the interaction between low-frequency and high-frequency parametric instabilites in multiple dimensions. Test simulations of stimulated Raman scattering, stimulated Brillouin scattering, and Langmuir decay instability are presented.

Key Words: massively parallel; fully kinetic; reduced-description; two dimensional; particle-in-cell; parametric instabilities; stimulated Brillouin scattering; stimulated Raman scattering; Langmuir decay instability.

1. INTRODUCTION

In inertial confinement fusion (ICF) applications, an external high-frequency monochromatic laser is employed to irradiate the plasma. The external monochromatic electromagnetic wave, due to its interaction with the plasma, can undergo parametric instabilities, which

0021-9991/99

decay into various combinations of high-frequency or low-frequency daughter waves [1]. Recent experiments [2, 3] and Zakharov simulations [4, 5] indicate that in ICF plasmas of interest, nonlinear processes such as the Langmuir decay instability (LDI) and Langmuir collapse can affect the growth and saturation of the stimulated Raman scattering (SRS) instability. Due to a multitude of spatial and temporal scales that exist in such plasmas and the fact that the external driving electromagnetic field is of high frequency, general-purpose explicit, implicit, and hybrid particle-in-cell (PIC) algorithms [6, 30] are either incapable of simulating the actual physics, or computationally inefficient. In recent works [31–33], a special-purpose hybrid PIC model was presented in which the electrons are modeled as an adiabatic fluid with an arbitrary ratio of specific heats γ, and the electromagnetic field model is based on a temporal envelope approximation. This hybrid PIC model was implemented in three dimensions on a CRAY-T3D with 512 processors and was shown to model ion Landau damping, finite-Debye-length effects, aperiodically driven stimulated Brillouin scattering (SBS), and the interaction between SBS and the filamentation instability (FI) correctly [31–33]. However, this hybrid model does not include electron kinetic effects and is therefore inadequate for situations in which high-frequency parametric instabilities, such as stimulated Raman scattering, play a significant role.

In this paper, we present a fully kinetic reduced-description particle-in-cell (RPIC) model in which low-frequency and high-frequency parametric instabilities and their interaction are modeled accurately and efficiently. It can be shown that in the limit where high-frequency instabilities are not important, RPIC reduces to the aforementioned hybrid model [31–33].

RPIC treats electrons and ions as discrete finite-size particles, allowing linear and nonlinear kinetic effects to be modeled correctly for both electrons and ions. The Poisson equation is solved to ensure that space-charge effects are included. The electromagnetic field is modeled using a temporal envelope representation that results in three coupled Schrödinger-like equations for the envelopes of: (1) the incident and SBS-scattered electromagnetic field, (2) the frequency-downshifted SRS-scattered electromagnetic field, and (3) the frequency-upshifted SRS-scattered electromagnetic field. A novel feature of RPIC is the method of extracting the temporal electron density envelopes from the instantaneous electron density which, in turn, is obtained by interpolating from the particles onto the computational mesh. It is important to note here that unlike standard explicit PIC models in which the electrons and ions are advanced in phase-space using the same electric field, RPIC legislates that the ion response has no high-frequency components. This is justified because the ions are too massive to have any appreciable high-frequency response. The elimination of high-frequency components from the ion response is a unique feature of RPIC and is a crucial element in allowing secondary parametric decay processes to be modeled accurately. Without the elimination of high-frequency components from the ion response, high-frequency scattering of low-frequency ion acoustic waves would tend to obscure these secondary decay processes. It has been shown in a recent work of Sanbonmatsu *et al.* [34] that there is excellent quantitative agreement between RPIC and a quasilinear Zakharov (fluid) model in the weakly driven regime where the Zakharov model is generally anticipated to be valid. This quantitative agreement includes Langmuir wave spectra, acoustic wave spectra, electron distribution function, and time-history of the Langmuir wave energy. Such quantitative agreement has been an elusive goal of plasma simulations of nonlinear parametric processes occuring in ICF plasmas until now.

The rest of this paper is divided into six sections. In Section 2, we describe the physical model appropriate for simulating parametric instabilities with both high-frequency and

low-frequency daughter waves. The conservation laws which RPIC obeys are shown and discussed in Section 3. In Section 4, the temporal mean-square noise spectra are characterized both analytically and numerically. This is of importance because in the aforementioned work of Sanbonmatsu *et al.* [34], where quantitative comparisons between ASPEN and a quasilinear Zakharov model were made, one must be able to characterize the noise spectra in ASPEN so that these spectra can be imposed as noise sources in the quasilinear Zakharov simulations. In Section 5, the numerical algorithm for advancing the governing equations in time and its numerical properties are discussed. In Section 6, test simulations of undriven Landau-damped Langmuir waves and of SRS and the Langmuir decay instability (LDI) are presented. Section 7 is a summary of our results and conclusions based on these results.

2. RPIC MODEL

In the presence of an electromagnetic pump wave of frequency ω_0, the self-consistent vector potential, scalar potential, and density response of a plasma with uniform background plasma frequency ω_{pe0} can be written as

$$\begin{aligned}
\mathbf{A}(\mathbf{x}, t) &= \frac{1}{2}\left(\mathbf{a}_m(\mathbf{x}, t)\mathrm{e}^{-i\omega_m t} + \mathbf{a}_m^*(\mathbf{x}, t)\mathrm{e}^{i\omega_m t}\right), \\
\phi(\mathbf{x}, t) &= \phi_S(\mathbf{x}, t) + \frac{1}{2}\left(\phi_F(\mathbf{x}, t)\mathrm{e}^{-i\omega_{pe0} t} + \phi_F^*(\mathbf{x}, t)\mathrm{e}^{i\omega_{pe0} t}\right), \\
n_e(\mathbf{x}, t) &= n_{eS}(\mathbf{x}, t) + \frac{1}{2}\left(n_{eF}(\mathbf{x}, t)\mathrm{e}^{-i\omega_{pe0} t} + n_{eF}^*(\mathbf{x}, t)\mathrm{e}^{i\omega_{pe0} t}\right),
\end{aligned} \tag{1}$$

where the integer index $m = -1, 0, 1$, $\omega_m = \omega_0 + m\omega_{pe0}$, and the convention of summing over repeated indices is assumed. The temporal envelopes $\mathbf{a}_m$, ϕ_F, and n_{eF} are complex-valued and are assumed to vary on a time scale much longer than $2\pi/\omega_{pe0}$. The envelope $\mathbf{a}_0(\mathbf{x}, t)$ represents the incident electromagnetic field and the SBS-scattered electromagnetic field. The envelopes $\mathbf{a}_{-1}(\mathbf{x}, t)$ and $\mathbf{a}_1(\mathbf{x}, t)$ represent the scattered electromagnetic field due to frequency-downshifted and frequency-upshifted SRS, respectively. ϕ_S and ϕ_F represent electrostatic potentials associated with low-frequency and high-frequency waves, respectively, including ion acoustic waves (IAWs) and Langmuir waves (LWs). $n_{eS}(\mathbf{x}, t)$ includes the background electron density and any low-frequency electron density perturbation. $n_{eF}(\mathbf{x}, t)$ is the electron density associated with high-frequency waves. It is noted here that in writing Eqs. (1), one has tacitly neglected harmonic generation of both the light waves and LWs. In fact, for situations of interest to the ICF effort, the laser intensity is not sufficiently high to make harmonic generation important. In particular, in writing Eqs. (1), one assumes that the electron density response can be expressed as a linear combination of IAWs and LWs. In order for the model to be numerically tractable, one must, therefore, be able to extract the temporal envelopes n_{eS} and n_{eF} from the instantaneous electron density n_e which, in turn, is computed by interpolating particle data onto the computational mesh. The task of calculating n_{eS} and n_{eF} from n_e is a novel feature of this work and will be discussed subsequently. It is worth noting that by applying the temporal envelope approximation, one has eliminated the laser timescale from the model, and the time step of the simulation is limited by the Courant condition of the thermal electrons, whereas with standard explicit PIC models, the time step of the simulation is limited by the Courant condition of the light

wave. Thus, the CPU time required by RPIC is less than that of standard explicit PIC models by the ratio of the electron thermal speed to the speed of light. Typically, this saving is about one order of magnitude.

Unlike standard PIC models in which the electrons and ions are advanced in phase-space using the same electric field, RPIC advances the particles as follows:

$$\begin{aligned} m_e \frac{d\mathbf{u}_e}{dt} &= e\nabla\phi - \frac{e^2}{4m_e c^2}\nabla\left(\mathbf{a}_m \cdot \mathbf{a}_l^* \mathrm{e}^{-i(m-l)\omega_{pe0}t}\right), \\ \frac{d\mathbf{x}_e}{dt} &= \mathbf{u}_e, \\ m_i \frac{d\mathbf{u}_i}{dt} &= -eZ_i\nabla\phi_S - \frac{e^2 Z_i^2}{4m_i c^2}\nabla(\mathbf{a}_m \cdot \mathbf{a}_m), \\ \frac{d\mathbf{x}_i}{dt} &= \mathbf{u}_i. \end{aligned} \tag{2}$$

In writing Eqs. (2), one has assumed that the electrons are nonrelativistic. In Eqs. (2), the electron response has been averaged over the laser time scale, and the ion response has likewise been averaged over the electron time scale [31–33]. It can be shown, within the framework of kinetic theory, that by eliminating the high-frequency components of the electric field under whose influence the ions are advanced, one has: (a) eliminated ion–electron collisions completely and (b) reduced the ion velocity diffusion substantially. As a result, secondary decay processes such as LDI can be modeled accurately in an efficient manner. In fact, it has been shown [34] that our PIC model can capture at least three steps of secondary decays beyond the primary decay. The elimination of ion–electron collision is justified because the plasmas under consideration are sufficiently hot that they are essentially collisionless.

The electron and ion number densities are computed by interpolating particle data,

$$\begin{aligned} -en_e(\mathbf{x}, t) &= \sum_{p\in e} q_p S(\mathbf{x} - \mathbf{x}_p(t)), \\ eZ_i n_i(\mathbf{x}, t) &= \sum_{p\in i} q_p S(\mathbf{x} - \mathbf{x}_p(t)), \end{aligned} \tag{3}$$

where $S(\mathbf{x})$ is the particle interpolation function and is taken to be the biquadratic B-spline of compact support.

The scalar potentials are obtained from Poisson's equations,

$$\begin{aligned} \nabla^2\phi &= 4\pi e\left(n_e - \sum_i Z_i n_i\right), \\ \nabla^2\phi_S &= 4\pi e\left(n_{eS} - \sum_i Z_i n_i\right), \end{aligned} \tag{4}$$

where one has made use of the fact that the ion density in this model does not have a high-frequency component.

The self-consistent vector potential $\mathbf{A}$ described in Eqs. (1) can be shown to excite high-frequency electron and ion motions with velocities $\mathbf{u}_{Te} = e\mathbf{A}/m_e c$ and $\mathbf{u}_{Ti} = -Z_i e\mathbf{A}/m_i c$

[31], which in turn give rise to currents of the form $\mathbf{J}_e = e^2 n_e \mathbf{A}/m_e c$ and $\mathbf{J}_i = Z_i^2 e^2 n_i \mathbf{A}/m_i c$. The net transverse current is obtained by summing over the individual currents and by projecting out any longitudinal contribution as follows:

$$\mathbf{J}_T \approx -\frac{1}{4\pi c}\left[4\pi e^2\left(\frac{n_e}{m_e}+\sum_i \frac{Z_i^2 n_i}{m_i}\right)\mathbf{A} - \nabla\chi\right],$$
$$\nabla^2\chi = 4\pi e^2 \mathbf{A}\cdot\nabla\left(\frac{n_e}{m_e}+\sum_i \frac{Z_i^2 n_i}{m_i}\right).$$

Here, c is the speed of light. The index i denotes the ion species. Z_i, m_i, and n_i are the ionization state, ionic mass, and number density of the ith ion species. Likewise, m_e and n_e are the electronic mass and electron number density, respectively. It is noted that χ is defined such that $\nabla\cdot\mathbf{J}_T = \nabla\cdot\mathbf{A} = 0$.

Substituting the above expression for $\mathbf{J}_T$ into Ampere's law, $\nabla\times\mathbf{B} = (4\pi/c)\mathbf{J}_T + (1/c)\partial\mathbf{E}_T/\partial t$, neglecting the second-order temporal derivatives of the field envelopes $\mathbf{a}_m$ and harmonic generation, and separating frequency components, one obtains three coupled Schrödinger-like equations,

$$\begin{aligned}
&i\left(\frac{2\omega_0}{c^2}\right)\frac{\partial\mathbf{a}_0}{\partial t} + \nabla^2\mathbf{a}_0 + \frac{1}{c^2}\nabla\chi_0 + \frac{4\pi e^2}{c^2}\left(\frac{n_0 - n_{eS}}{m_e} - \sum_i \frac{Z_i^2 n_i}{m_i}\right)\mathbf{a}_0 \\
&\quad = \frac{4\pi e^2}{2m_e c^2}(n_{eF}\mathbf{a}_{-1} + n_{eF}^*\mathbf{a}_1) - \frac{1}{2c^2}\nabla\xi_0, \\
&i\left(\frac{2\omega_{-1}}{c^2}\right)\frac{\partial\mathbf{a}_{-1}}{\partial t} + \nabla^2\mathbf{a}_{-1} + \frac{1}{c^2}\nabla\chi_{-1} + \frac{4\pi e^2}{c^2}\left(\frac{n_{-1} - n_{eS}}{m_e} - \sum_i \frac{Z_i^2 n_i}{m_i}\right)\mathbf{a}_{-1} \\
&\quad = \frac{4\pi e^2}{2m_e c^2} n_{eF}^*\mathbf{a}_0 - \frac{1}{2c^2}\nabla\xi_{-1}, \\
&i\left(\frac{2\omega_1}{c^2}\right)\frac{\partial\mathbf{a}_1}{\partial t} + \nabla^2\mathbf{a}_1 + \frac{1}{c^2}\nabla\chi_1 + \frac{4\pi e^2}{c^2}\left(\frac{n_1 - n_{eS}}{m_e} - \sum_i \frac{Z_i^2 n_i}{m_i}\right)\mathbf{a}_1 \\
&\quad = \frac{4\pi e^2}{2m_e c^2} n_{eF}\mathbf{a}_0 - \frac{1}{2c^2}\nabla\xi_1,
\end{aligned} \tag{5}$$

with $4\pi e^2 n_m/m_e \equiv \omega_m^2$, $m = -1, 0, 1$. The scalars χ_m and ξ_m are defined such that $\nabla\cdot\mathbf{a}_m = 0$ and are as follows:

$$\begin{aligned}
\nabla^2\chi_m &\equiv 4\pi e^2 \mathbf{a}_m\cdot\nabla\left(\frac{n_{eS}}{m_e} + \sum_i \frac{Z_i^2 n_i}{m_i}\right), \\
\nabla^2\xi_0 &\equiv \frac{4\pi e^2}{m_e}(\mathbf{a}_{-1}\cdot\nabla n_{eF} + \mathbf{a}_1\cdot\nabla n_{eF}^*), \\
\nabla^2\xi_{-1} &\equiv \frac{4\pi e^2}{m_e}\mathbf{a}_0\cdot\nabla n_{eF}^*, \\
\nabla^2\xi_1 &\equiv \frac{4\pi e^2}{m_e}\mathbf{a}_0\cdot\nabla n_{eF}.
\end{aligned} \tag{6}$$

It is noted that in the 2D geometry considered in Section 6B (and in 1D) the scalars χ_m and ξ_m can be taken to be zero. The temporal envelopes ϕ_F and n_{eF} are computed as follows:

$$\begin{aligned} n_{eF} &\approx \mathrm{e}^{i\omega_{pe0}t}\left[-\frac{1}{i\omega_{pe0}}\frac{\partial n_e}{\partial t} + (n_e - n_{eS})\right], \\ \phi_F &\approx \mathrm{e}^{i\omega_{pe0}t}\left[-\frac{1}{i\omega_{pe0}}\frac{\partial \phi}{\partial t} + (\phi - \phi_S)\right]. \end{aligned} \tag{7}$$

Equations (7) are the result of simple manipulation of Eqs. (1) where higher-order harmonics have been neglected, and the assumption of the slow temporal variation of ϕ_F and n_{eF} on the time scale of $2\pi/\omega_{pe0}$ is explicitly invoked. Closure of the model is obtained with the following equations,

$$\begin{aligned} & e\phi_S - \frac{e^2}{4m_e c^2}\,\mathbf{a}_m \cdot \mathbf{a}_m^* - f(\gamma, n_{eS}) \\ & - \frac{1}{4m_e\omega_{pe0}^2}\left|\nabla\left[e\phi_F - \frac{e^2}{2m_e c^2}(\mathbf{a}_0 \cdot \mathbf{a}_{-1}^* + \mathbf{a}_0^* \cdot \mathbf{a}_1)\right]\right|^2 = \alpha(t), \end{aligned} \tag{8}$$

$$f(\gamma, n_{eS}) = \begin{cases} T_{e0}\ln\left(\frac{n_{eS}}{n_{e0}}\right) & \text{if } \gamma = 1 \\ T_{e0}\left(\frac{\gamma}{\gamma-1}\right)\left(\frac{n_{eS}}{n_{e0}}\right)^{\gamma-1} & \text{if } \gamma \neq 1 \end{cases}, \tag{9}$$

where α is a constant of spatial integration and is therefore only a function of t. In our model, α is chosen such that global charge neutrality is ensured; i.e.,

$$\int \nabla\phi_S \cdot d\boldsymbol{\sigma} = 0. \tag{10}$$

Here, n_{e0} and T_{e0} are the initial electron density and temperature and $d\boldsymbol{\sigma}$ a surface area element. A detailed derivation of the closure equations, Eqs. (8), (9), is tedious and has been deferred to Appendix A in order to improve the readibility of the paper. Equations (7)–(9), which allow the decompositions of the electron density and electrostatic potential into their respective low-frequency and high-frequency components, are critical steps in the RPIC model. Without Eqs. (7)–(9), the concept of temporal envelope representation of the electromagnetic waves cannot be applied toward PIC modeling of parametric instabilities.

In summary, Eqs. (2)–(10) constitute our physical model. Equations (3)–(10) are solved self-consistently to obtain the vector and scalar potentials, and Eqs. (2) are used to advance the electrons and ions in phase-space in response to the presence of these forces.

3. CONSERVATION LAWS

The model presented in Section 2 obeys certain conservation laws which are not immediately obvious. Here, three conservation laws can be derived from the model: (1) conservation of the number of photons, (2) conservation of energy, and (3) conservation of momentum. Conservation of charge is trivially satisfied and will not be derived. It is noted here that it is important that the model conserves momentum because momentum imparted on the particles by the light waves, over a sufficiently long time, can affect plasma hydrodynamic motion and the evolution of parametric instabilities [35].

The conservation laws can be derived from our model, Eqs. (2)–(10), using the standard approach in classical electrodynamics, and the results are as follows,

$$\frac{d}{dt}\left(\frac{E_m}{\omega_m}\right) + \int \frac{\mathbf{F}_m}{\omega_m} \cdot d\boldsymbol{\sigma} = 0, \tag{11}$$

$$\frac{d}{dt}(E_{KL} + E_{KT} + E_\phi + E_1 + E_0 + E_{-1}) + \int (\mathbf{F}_{KL} + \mathbf{F}_{KT} + \mathbf{F}_\phi + \mathbf{F}_1 + \mathbf{F}_0 + \mathbf{F}_{-1}) \cdot d\boldsymbol{\sigma} = 0, \tag{12}$$

$$\frac{d}{dt}(\mathbf{P}_K + \mathbf{P}) + \int d\boldsymbol{\sigma} \cdot (\boldsymbol{\Gamma}_K + \boldsymbol{\Gamma}) = 0, \tag{13}$$

where the various momenta, energies, and fluxes are defined as follows:

$$\mathbf{e}_0 \equiv i\omega_0 \mathbf{a}_0/c,$$

$$\mathbf{e}_1 \equiv i\omega_1 \mathbf{a}_1/c,$$

$$\mathbf{e}_{-1} \equiv i\omega_{-1} \mathbf{a}_{-1}/c,$$

$$\mathbf{b}_m \equiv \nabla \times \mathbf{a}_m, \quad m = -1, 0, 1,$$

$$E_m \equiv \int \frac{|\mathbf{e}_m|^2}{8\pi}\, d^3\mathbf{x}, \quad m = -1, 0, 1,$$

$$\mathbf{F}_0 \equiv \frac{c}{16\pi}\left([\nabla \mathbf{a}_0^*] \cdot \mathbf{e}_0 + [\nabla \mathbf{a}_0] \cdot \mathbf{e}_0^* + \frac{1}{c^2}\left[\chi_0^* + \frac{1}{2}\xi_0^*\right]\mathbf{e}_0 + \frac{1}{c^2}\left[\chi_0 + \frac{1}{2}\xi_0\right]\mathbf{e}_0^*\right),$$

$$\mathbf{F}_1 \equiv \frac{c}{16\pi}\left([\nabla \mathbf{a}_1^*] \cdot \mathbf{e}_1 + [\nabla \mathbf{a}_1] \cdot \mathbf{e}_1^* + \frac{1}{c^2}\left[\chi_1^* + \frac{1}{2}\xi_1^*\right]\mathbf{e}_1 + \frac{1}{c^2}\left[\chi_1 + \frac{1}{2}\xi_1\right]\mathbf{e}_1^*\right),$$

$$\mathbf{F}_{-1} \equiv \frac{c}{16\pi}\left([\nabla \mathbf{a}_{-1}^*] \cdot \mathbf{e}_{-1} + [\nabla \mathbf{a}_{-1}] \cdot \mathbf{e}_{-1}^* + \frac{1}{c^2}\left[\chi_{-1}^* + \frac{1}{2}\xi_{-1}^*\right]\mathbf{e}_{-1} + \frac{1}{c^2}\left[\chi_{-1} + \frac{1}{2}\xi_{-1}\right]\mathbf{e}_{-1}^*\right),$$

$$E_\phi \equiv \frac{1}{8\pi}\int \left(|\nabla \phi_S|^2 + \frac{1}{2}|\nabla \phi_F|^2\right) d^3\mathbf{x},$$

$$\mathbf{F}_\phi \equiv -\langle \phi n_e \mathbf{U}_e \rangle + \sum_i e\phi_S Z_i n_i \mathbf{U}_i - \frac{1}{4\pi}\left(\phi_S \nabla \frac{\partial \phi_S}{\partial t} + \frac{i\omega_{pe0}}{4}[\phi_F \nabla \phi_F^* - \phi_F^* \nabla \phi_F]\right),$$

$$E_{KL} \equiv \left\langle \sum_{p\in e} \frac{1}{2} m_p |\mathbf{u}_p|^2 + \sum_i \sum_{p\in i} \frac{1}{2} m_p |\mathbf{u}_p|^2 \right\rangle,$$

$$\mathbf{F}_{KL} \equiv \left\langle \sum_{p\in e} \frac{1}{2} m_p |\mathbf{u}_p|^2 \mathbf{u}_p \delta(\mathbf{x} - \mathbf{x}_p) + \sum_i \sum_{p\in i} \frac{1}{2} m_p |\mathbf{u}_p|^2 \mathbf{u}_p \delta(\mathbf{x} - \mathbf{x}_p) \right\rangle,$$

$$E_{KT} \equiv \int \frac{1}{16\pi c^2}\left(\frac{4\pi e^2 n_{eS}}{m_e} + \sum_i \frac{4\pi e^2 Z_i^2 n_i}{m_i}\right) \mathbf{a}_m \cdot \mathbf{a}_m^*\, d^3\mathbf{x},$$

$$\mathbf{F}_{KT} \equiv \frac{1}{16\pi c^2}\left\langle \frac{4\pi e^2 n_e}{m_e}\mathbf{U}_e\mathbf{a}_m\cdot\mathbf{a}_l^* e^{-i(m-l)\omega_{pe0}t}\right\rangle + \frac{\mathbf{a}_m\cdot\mathbf{a}_m^*}{16\pi c^2}\sum_i \frac{4\pi e^2 Z_i^2 n_i}{m_i}\mathbf{U}_i,$$

$$\mathbf{P}_K \equiv \left\langle \sum_{p\in e} m_p\mathbf{u}_p + \sum_i\sum_{p\in i} m_p\mathbf{u}_p\right\rangle,$$

$$\mathbf{\Gamma}_K \equiv \left\langle \sum_{p\in e} m_p\mathbf{u}_p\mathbf{u}_p\delta(\mathbf{x}-\mathbf{x}_p) + \sum_i\sum_{p\in i} m_p\mathbf{u}_p\mathbf{u}_p\delta(\mathbf{x}-\mathbf{x}_p)\right\rangle,$$

$$\mathbf{P} \equiv \int \frac{1}{16\pi c}(\mathbf{e}_m\times\mathbf{b}_m^* + \mathbf{e}_m^*\times\mathbf{b}_m)\,d^3\mathbf{x},$$

$$\begin{aligned}\mathbf{\Gamma} \equiv \frac{1}{16\pi}\Bigg(&\{\mathbf{b}_m,\mathbf{b}_m^*\}+\{\mathbf{e}_m,\mathbf{e}_m^*\}-[\nabla\times\mathbf{b}_m]\mathbf{a}_m^*-[\nabla\times\mathbf{b}_m^*]\mathbf{a}_m\\ &+\frac{1}{c^2}\left[\mathbf{a}_m\cdot\nabla\left(\chi_m^*+\frac{1}{2}\xi_m^*\right)+\mathbf{a}_m^*\cdot\nabla\left(\chi_m+\frac{1}{2}\xi_m\right)\right]\mathbf{I}\\ &-\frac{1}{c^2}\left[\mathbf{a}_m\nabla\left(\chi_m^*+\frac{1}{2}\xi_m^*\right)+\mathbf{a}_m^*\nabla\left(\chi_m+\frac{1}{2}\xi_m\right)\right]\Bigg)\\ &+\frac{1}{8\pi}\{\nabla\phi_S,\nabla\phi_S\}+\frac{1}{16\pi}\{\nabla\phi_F,\nabla\phi_F\}.\end{aligned}$$

The densities n_e and n_i are given by Eqs. (3), $n_{e,i}\mathbf{U}_{e,i}\equiv\sum_{p\in e,i}\mathbf{u}_p\delta(\mathbf{x}-\mathbf{x}_p)$, $\langle\cdots\rangle$ denotes temporal averaging over the electron plasma timescale, $\{\mathbf{a},\mathbf{b}\}\equiv(\mathbf{a}\cdot\mathbf{b})\mathbf{I}-\mathbf{ab}-\mathbf{ba}$, and $\mathbf{I}$ is the unit dyad. $d\boldsymbol{\sigma}$ is a surface area element. Equations (11), (12), and (13) are conservation laws for the number of photons (if both sides of (11) are divided by $\hbar$), total energy, and total momentum, respectively. It is noted that in writing Eqs. (11)–(13), one has assumed $|\partial n_{eS}/\partial t|\ll|\partial n/\partial t|$, $|\partial n_{eF}/\partial t|\ll\omega_{pe0}|n_{eF}|$, and $|\partial\mathbf{a}_m/\partial t|\ll\omega_{pe0}|\mathbf{a}_m|$. These assumptions are, of course, consistent with the validity of the envelope representation on which RPIC is based.

4. NUMERICAL NOISE

A detailed analysis of the density and electrostatic potential fluctuations for RPIC can be found in Appendix B. In particular, temporal mean-square noise spectra for the quantities n_i, n_e, n_{eS}, n_{eF}, ϕ_{eS}, and ϕ_{eF} are derived analytically by solving the linearized Vlasov equations (see Eqs. (B.2) and (B.3)), taking into account the facts that the computational mesh is discrete and that the particles have a finite spatial extent. These derived temporal mean-square noise spectra are then compared to simulation results. The results are important because in the aforementioned work of Sanbonmatsu *et al.* [34] where quantitative comparisons of ASPEN simulations with quasilinear Zakharov simulations were made, one must be able to characterize PIC noise spectra so that these spectra can be imposed as noise sources in the Zakharov simulations. Furthermore, because the linear growth phase of parametric instabilities is sensitive to the noise spectrum, it is imperative that the noise spectrum be known.

Figure 1 is a comparison between Eqs. (B.2) and (B.3) and 1D numerical simulations in which the external electromagnetic field is absent and indicate excellent agreement between

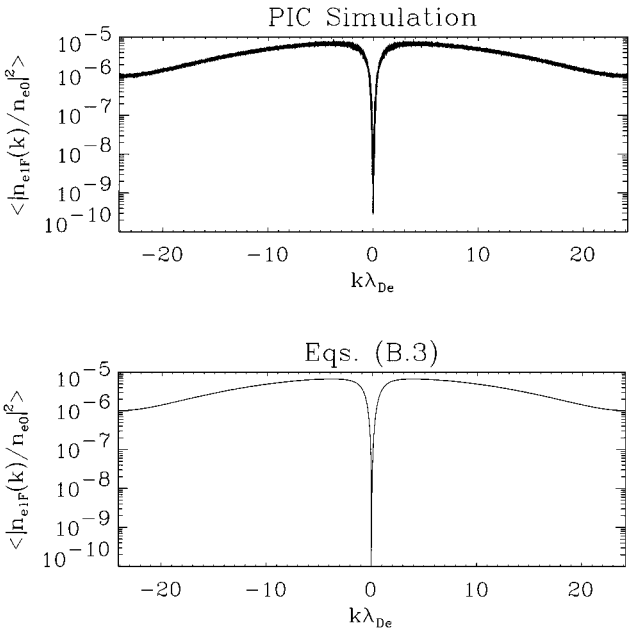

FIG. 1. Temporal mean-square high-frequency electron density spectrum with $L_x/\lambda_{De} = 4260$, $\delta x/\lambda_{De} = 0.13$, $T_i/T_e = 0.1$, $m_i/m_e = 1836$. Both electrons and ions are represented by four finite-size particles per computational cell.

theory and simulations. The spectra obtained from the simulation are averaged over a period of 2500 plasma period. Two-dimensional simulations (not shown) are also in good agreement with Eqs. (B.2) and (B.3).

5. NUMERICAL ALGORITHM

A temporal discretization scheme and its accompanying nonlinear numerical analysis are presented in which the numerical solutions are shown to be stable, provided that $\omega_{pe}\delta t < 1$ and that the Courant condition for the electrons is satisfied. The iterative procedure for solving the time-discrete equations is discussed. Two-dimensional spatial discretization of the equations and parallelization-related issues, such as domain decomposition, will also be discussed.

Each particle carries a charge q_p, position $\mathbf{x}_p$, and velocity u_p. Associated with each particle is an interpolation function $S(\mathbf{x} - \mathbf{x}_p)$ that determines how the particle charges are interpolated onto the computational mesh, as indicated in Eqs. (3). In our two-dimensional Cartesian implementation of Eqs. (2)–(10), $S(\mathbf{x})$ is chosen to be a biquadratic B-spline.

A. *Temporal Discretization*

Using the leapfrog algorithm in which the pair of variables $\mathbf{x}_p$ and $\mathbf{u}_p$ are advanced alternately in time, the particle equations of motion, Eqs. (2), are approximated as

follows:

$$\begin{aligned}
\frac{\mathbf{u}_{pe}^{(\mathrm{n}+1/2)}-\mathbf{u}_{pe}^{(\mathrm{n}-1/2)}}{\delta t} &= -\frac{q_p}{m_p}\nabla\left(\phi^{(\mathrm{n})}+\frac{q_p}{4m_pc^2}\mathbf{a}_m^{(\mathrm{n})}\cdot\mathbf{a}_l^{*(\mathrm{n})}\mathrm{e}^{-i(m-l)\omega_{pe0}t^{(\mathrm{n})}}\right),\\
\frac{\mathbf{x}_{pe}^{(\mathrm{n}+1)}-\mathbf{x}_{pe}^{(\mathrm{n})}}{\delta t} &= \mathbf{u}_{pe}^{(\mathrm{n}+1/2)},\\
\frac{\mathbf{u}_{pi}^{(\mathrm{n}+1/2)}-\mathbf{u}_{pi}^{(\mathrm{n}-1/2)}}{\delta t} &= -\frac{q_p}{m_p}\nabla\left(\phi_S^{(\mathrm{n})}+\frac{q_p}{4m_pc^2}\mathbf{a}_m^{(\mathrm{n})}\cdot\mathbf{a}_m^{*(\mathrm{n})}\right),\\
\frac{\mathbf{x}_{pi}^{(\mathrm{n}+1)}-\mathbf{x}_{pi}^{(\mathrm{n})}}{\delta t} &= \mathbf{u}_{pi}^{(\mathrm{n}+1/2)}.
\end{aligned} \tag{14}$$

The superscripts denote the time level at which the physical variables are evaluated, and $t^{(\mathrm{n})}=n\delta t$.

The electron and ion number densities are obtained by evaluating Eqs. (3) at discrete mesh points:

$$\begin{aligned}
-en_e^{(\mathrm{n})}(\mathbf{x}) &= \sum_{p\in e} q_p S\big(\mathbf{x}-\mathbf{x}_p^{(\mathrm{n})}\big),\\
eZ_in_i^{(\mathrm{n})}(\mathbf{x}) &= \sum_{p\in i} q_p S\big(\mathbf{x}-\mathbf{x}_p^{(\mathrm{n})}\big).
\end{aligned} \tag{15}$$

The scalar potentials $\phi^{(\mathrm{n})}$ and $\phi_S^{(\mathrm{n})}$ are obtained by evaluating Eqs. (4) at discrete time levels:

$$\begin{aligned}
\nabla^2\phi^{(\mathrm{n})} &= 4\pi e\left(n_e^{(\mathrm{n})}-\sum_i Z_in_i^{(\mathrm{n})}\right),\\
\frac{1}{2}\nabla^2\big(\phi_S^{(\mathrm{n})}+\phi_S^{(\mathrm{n}-1)}\big) &= 4\pi e\left(n_{eS}^{(\mathrm{n}-1/2)}-\frac{1}{2}\sum_i Z_i\big[n_i^{(\mathrm{n})}+n_i^{(\mathrm{n}-1)}\big]\right).
\end{aligned} \tag{16}$$

The Schrödinger equations, Eqs. (5), are discretized using the Crank–Nicholson method [31–33],

$$\begin{aligned}
&i\left(\frac{2\omega_0}{c^2}\right)\frac{\mathbf{a}_0^{(\mathrm{n})}-\mathbf{a}_0^{(\mathrm{n}-1)}}{\delta t}+\nabla^2\mathbf{a}_0^{(\mathrm{n}-1/2)}+\frac{1}{2c^2}\nabla\xi_0^{(\mathrm{n}-1/2)}+\frac{4\pi e^2}{m_ec^2}\big(n_0-n_{eS}^{(\mathrm{n}-1/2)}\big)\mathbf{a}_0^{(\mathrm{n}-1/2)}\\
&\quad+\frac{1}{c^2}\nabla\chi_0^{(\mathrm{n}-1/2)}=\frac{2\pi e^2}{m_ec^2}n_{eF}^{(\mathrm{n}-1/2)}\mathbf{a}_{-1}^{(\mathrm{n}-1/2)}+\frac{2\pi e^2}{m_ec^2}n_{eF}^{*(\mathrm{n}-1/2)}\mathbf{a}_1^{(\mathrm{n}-1/2)},\\
&i\left(\frac{2\omega_{-1}}{c^2}\right)\frac{\mathbf{a}_{-1}^{(\mathrm{n})}-\mathbf{a}_{-1}^{(\mathrm{n}-1)}}{\delta t}+\nabla^2\mathbf{a}_{-1}^{(\mathrm{n}-1/2)}+\frac{1}{2c^2}\nabla\xi_{-1}^{(\mathrm{n}-1/2)}+\frac{4\pi e^2}{m_ec^2}\big(n_{-1}-n_{eS}^{(\mathrm{n}-1/2)}\big)\mathbf{a}_{-1}^{(\mathrm{n}-1/2)}\\
&\quad+\frac{1}{c^2}\nabla\chi_{-1}^{(\mathrm{n}-1/2)}=\frac{2\pi e^2}{m_ec^2}n_{eF}^{*(\mathrm{n}-1/2)}\mathbf{a}_0^{(\mathrm{n}-1/2)},\\
&i\left(\frac{2\omega_1}{c^2}\right)\frac{\mathbf{a}_1^{(\mathrm{n})}-\mathbf{a}_1^{(\mathrm{n}-1)}}{\delta t}+\nabla^2\hat{\mathbf{a}}_1+\frac{1}{2c^2}\nabla\xi_1^{(\mathrm{n}-1/2)}+\frac{4\pi e^2}{c^2}\big(n_1-n_{eS}^{(\mathrm{n}-1/2)}\big)\mathbf{a}_1^{(\mathrm{n}-1/2)}\\
&\quad+\frac{1}{c^2}\nabla\chi_1^{(\mathrm{n}-1/2)}=\frac{2\pi e^2}{m_ec^2}n_{eF}^{(\mathrm{n}-1/2)}\mathbf{a}_0^{(\mathrm{n}-1/2)},
\end{aligned} \tag{17}$$

where $\mathbf{a}_m^{(n-1/2)} \equiv (\mathbf{a}_m^{(n)} + \mathbf{a}_m^{(n-1)})/2$ and $n_{eS}^{(n-1/2)} \equiv (n_{eS}^{(n)} + n_{eS}^{(n-1)})/2$. It is noted that with very little loss of accuracy, terms of order m_e/m_i have been neglected. $\hat{\chi}_m$ and $\hat{\xi}_m$ are defined as follows:

$$\begin{aligned}
\nabla^2 \chi_m^{(n-1/2)} &\equiv \frac{4\pi e^2}{m_e} \mathbf{a}_m^{(n-1/2)} \cdot \nabla n_{eS}^{(n-1/2)}, \\
\nabla^2 \xi_0^{(n-1/2)} &\equiv \frac{4\pi e^2}{m_e} \left(\mathbf{a}_{-1}^{(n-1/2)} \cdot \nabla n_{eF}^{(n-1/2)} + \mathbf{a}_1^{(n-1/2)} \cdot \nabla n_{eF}^{*(n-1/2)} \right), \\
\nabla^2 \xi_{-1}^{(n-1/2)} &\equiv \frac{4\pi e^2}{m_e} \mathbf{a}_0^{(n-1/2)} \cdot \nabla n_{eF}^{*(n-1/2)}, \\
\nabla^2 \xi_1^{(n-1/2)} &\equiv \frac{4\pi e^2}{m_e} \mathbf{a}_0^{(n-1/2)} \cdot \nabla n_{eF}^{(n-1/2)}.
\end{aligned} \tag{18}$$

Closure is obtained by evaluating Eqs. (7)–(10) at $t^{(n-1/2)}$:

$$\begin{aligned}
\phi_F^{(n-1/2)} &= e^{i\omega_{pe0} t^{(n-1/2)}} \left(-\frac{\phi^{(n)} - \phi^{(n-1)}}{i\omega_{pe0}\delta t} + \frac{\phi^{(n)} + \phi^{(n-1)}}{2} - \frac{\phi_S^{(n)} + \phi_S^{(n-1)}}{2} \right), \\
n_{eF}^{(n-1/2)} &= e^{i\omega_{pe0} t^{(n-1/2)}} \left(-\frac{n_e^{(n)} - n_e^{(n-1)}}{i\omega_{pe0}\delta t} + \frac{n_e^{(n)} + n_e^{(n-1)}}{2} - n_{eS}^{(n-1/2)} \right),
\end{aligned} \tag{19}$$

$$\begin{aligned}
&\frac{e\phi_S^{(n)} + e\phi_S^{(n-1)}}{2} - f\left(\gamma, n_{eS}^{(n-1/2)}\right) - \frac{e^2}{8m_e c^2} \left(\mathbf{a}_m^{(n)} \cdot \mathbf{a}_m^{*(n)} + \mathbf{a}_m^{(n-1)} \cdot \mathbf{a}_m^{*(n-1)} \right) \\
&- \frac{1}{4m_e\omega_{pe0}^2} \left| \nabla \left(e\phi_F^{(n-1/2)} - \frac{e^2}{4m_e c^2} \left[\mathbf{a}_0^{(n)} \cdot \mathbf{a}_{-1}^{*(n)} + \mathbf{a}_0^{(n-1)} \cdot \mathbf{a}_{-1}^{*(n-1)} \right. \right. \right. \\
&\left. \left. \left. + \mathbf{a}_0^{*(n)} \cdot \mathbf{a}_1^{(n)} + \mathbf{a}_0^{*(n-1)} \cdot \mathbf{a}_1^{(n-1)} \right] \right) \right|^2 = \alpha^{(n-1/2)},
\end{aligned} \tag{20}$$

$$f\left(\gamma, n_{eS}^{(n-1/2)}\right) = \begin{cases} T_{e0} \ln\left(\frac{n_{eS}^{(n-1/2)}}{n_{e0}} \right) & \text{if } \gamma = 1 \\ T_{e0} \left(\frac{\gamma}{\gamma - 1} \right) \left(\frac{n_{eS}^{(n-1/2)}}{n_{e0}} \right)^{\gamma - 1} & \text{if } \gamma \neq 1 \end{cases}, \tag{21}$$

$$\int \nabla \left(\frac{\phi_S^{(n)} + \phi_S^{(n-1)}}{2} \right) \cdot d\boldsymbol{\sigma} = 0. \tag{22}$$

Equations (14)–(22) represent the time-discrete form of our RPIC model. At time $t = t^{(n)}$, when the quantities $\mathbf{a}_m^{(n-1)}$, $\phi^{(n-1)}$, $\phi_S^{(n-1)}$, $n_e^{(n-1)}$, $n_i^{(n-1)}$, and particle velocities $\mathbf{u}_p^{(n-1/2)}$ and positions $\mathbf{x}_p^{(n)}$ are known, Eqs. (15) are evaluated in order to interpolate particle data onto the computational mesh to yield $n_e^{(n)}$ and $n_i^{(n)}$. Equations (16)–(22) are solved self-consistently for $\mathbf{a}_m^{(n)}$, $\phi^{(n)}$, $\phi_S^{(n)}$, $n_{eS}^{(n-1/2)}$, and $n_{eF}^{(n-1/2)}$. Equations (14) are then advanced in order to obtain the time-advanced velocities $\mathbf{u}_p^{(n+1/2)}$ and positions $\mathbf{x}_p^{(n+1)}$.

The leapfrog algorithm, Eqs. (14), is well known and has been shown in past literature to be numerically stable. We will therefore focus our attention on the nonlinear stability analysis of the coupled Schrödinger equations, Eqs. (17). Following the approach outlined

by Vu [31], Eqs. (17) can be recast as a time-discrete conservation law,

$$i\left(\frac{2\omega_m}{c^2\delta t}\right)\left(\left|\mathbf{a}_m^{(\mathrm{n})}\right|^2-\left|\mathbf{a}_m^{(\mathrm{n}-1)}\right|^2\right)+\nabla\cdot\mathbf{F}^{(\mathrm{n}-1/2)}=0,$$

$$\begin{aligned}\mathbf{F}^{(\mathrm{n}-1/2)}\equiv&\left[\nabla\mathbf{a}_m^{(\mathrm{n}-1/2)}\right]\cdot\mathbf{a}_m^{*(\mathrm{n}-1/2)}-\left[\nabla\mathbf{a}_m^{*(\mathrm{n}-1/2)}\right]\cdot\mathbf{a}_m^{(\mathrm{n}-1/2)}\\&+\frac{1}{c^2}\left(\chi_m^{(\mathrm{n}-1/2)}+\frac{1}{2}\xi_m^{(\mathrm{n}-1/2)}\right)\mathbf{a}_m^{*(\mathrm{n}-1/2)}-\frac{1}{c^2}\left(\chi_m^{*(\mathrm{n}-1/2)}+\frac{1}{2}\hat{\xi}_m^{*(\mathrm{n}-1/2)}\right)\mathbf{a}_m^{(\mathrm{n}-1/2)},\end{aligned}$$

where, as a reminder for the readers, the repeated index m is to be summed over. The above equation can be integrated over the volume of the simulation:

$$i\left(\frac{2\omega_m}{c^2\delta t}\right)\left(\int\left|\mathbf{a}_m^{(\mathrm{n})}\right|^2d^3\mathbf{x}-\int\left|\mathbf{a}_m^{(\mathrm{n}-1)}\right|^2d^3\mathbf{x}\right)+\int d\boldsymbol{\sigma}\cdot\mathbf{F}^{(\mathrm{n}-1/2)}=0.$$

It is noted here that the above equation is the time-discrete version of Eq. (11). When boundary conditions are such that there is no net flux $\mathbf{F}^{(\mathrm{n}-1/2)}$ crossing the simulation domain's boundary, the above equation reduces to the well-known Manley–Rowe relation [36]:

$$\omega_m\int\left|\mathbf{a}_m^{(\mathrm{n})}\right|^2d^3\mathbf{x}=\text{constant}.$$

Since each term of the left-hand side is positive-definite, the total energies contained in the incident and scattered waves are rigorously bounded, regardless of the time step δt. Therefore, Eqs. (17) are unconditionally stable.

B. *Spatial Discretization*

Consider a computational domain consisting of a rectangle with $0\le x\le L_x$ and $0\le y\le L_y$. The computational mesh is staggered and consists of $(\mathrm{N}_x-1)\times(\mathrm{N}_y-1)$ rectangular cells of equal size. $\mathbf{x}_{kl}^v$, the physical coordinate of the vertices of the computation cells, and $\mathbf{x}_{kl}^c$, the physical coordinate of the centers of the computational cells, are specified as follows,

$$\begin{aligned}\mathbf{x}_{kl}^v&=(k-1)\delta x\hat{\mathbf{e}}_x+(l-1)\delta y\hat{\mathbf{e}}_y,\\\mathbf{x}_{kl}^c&=\mathbf{x}_{kl}^v+\frac{\delta x}{2}\hat{\mathbf{e}}_x+\frac{\delta y}{2}\hat{\mathbf{e}}_y,\end{aligned}$$

where $\delta x\equiv L_x/(\mathrm{N}_x-1)$ and $\delta y\equiv L_y/(\mathrm{N}_y-1)$. Here, k and l are indices labeling the computational cells. It is noted here that this is the same geometry as that of an earlier Cartesian two-dimensional hybrid code [31].

The electron density n_e, density envelopes n_{eS} and n_{eF}, ion density n_i, scalar potential ϕ, scalar potential envelopes ϕ_S and ϕ_F, and electromagnetic field envelopes $\mathbf{a}_m$ with $m=-1, 0, 1$, are cell-centered quantities.

Equations (14), the time-discrete representation of our particle model, are spatially discretized by replacing the operator ∇ with the following numerical approximation,

$$\begin{aligned}[\nabla\mathrm{A}]\left(\mathbf{x}_{kl}^v\right)\approx&\left[\frac{\mathrm{A}\left(\mathbf{x}_{kl}^c\right)+\mathrm{A}\left(\mathbf{x}_{kl-1}^c\right)-\mathrm{A}\left(\mathbf{x}_{k-1l}^c\right)-\mathrm{A}\left(\mathbf{x}_{k-1l-1}^c\right)}{2\delta x}\right]\hat{\mathbf{e}}_x\\&+\left[\frac{\mathrm{A}\left(\mathbf{x}_{kl}^c\right)+\mathrm{A}\left(\mathbf{x}_{k-1l}^c\right)-\mathrm{A}\left(\mathbf{x}_{kl-1}^c\right)-\mathrm{A}\left(\mathbf{x}_{k-1l-1}^c\right)}{2\delta y}\right]\hat{\mathbf{e}}_y,\end{aligned}\tag{23}$$

where $\mathrm{A}(\mathbf{x}^c_{kl})$ is any cell-centered variable, e.g., the electrostatic potential $\phi^{(\mathrm{n})}$. It is clear from Eqs. (14) and (23) that when the scalar and vector potentials are cell-centered, as is the case here, the electric fields are vertex-centered. These vertex-centered electric fields are interpolated onto particle positions via bilinear B-spline of compact support [31]. These interpolated electric fields are subsequently used in Eqs. (14) to advance the particle positions and velocities in time.

Equations (15)–(22), the time-discrete representation of our field model, are spatially discretized by replacing the operators ∇ and ∇^2 with the following second-order numerical approximations:

$$
\begin{aligned}
[\nabla \mathrm{A}]\left(\mathbf{x}^c_{kl}\right) &\approx \left[\frac{\mathrm{A}\left(\mathbf{x}^c_{k+1l}\right) - \mathrm{A}\left(\mathbf{x}^c_{k-1l}\right)}{2\delta x}\right]\hat{\mathbf{e}}_x + \left[\frac{\mathrm{A}\left(\mathbf{x}^c_{kl+1}\right) - \mathrm{A}\left(\mathbf{x}^c_{kl-1}\right)}{2\delta y}\right]\hat{\mathbf{e}}_y, \\
\left[\nabla^2 \mathrm{A}\right]\left(\mathbf{x}^c_{kl}\right) &\approx \frac{\mathrm{A}\left(\mathbf{x}^c_{k+1l}\right) - 2\mathrm{A}\left(\mathbf{x}^c_{kl}\right) + \mathrm{A}\left(\mathbf{x}^c_{k-1l}\right)}{(\delta x)^2} + \frac{\mathrm{A}\left(\mathbf{x}^c_{kl+1}\right) - 2\mathrm{A}\left(\mathbf{x}^c_{kl}\right) + \mathrm{A}\left(\mathbf{x}^c_{kl-1}\right)}{(\delta y)^2}.
\end{aligned}
\tag{24}
$$

It is noted parenthetically that since no spatial enveloping is employed in the RPIC model, the grid resolution requirement for RPIC is the same as that of standard explicit PIC codes, i.e., the spatial grid size has to resolve the shortest wavelength of interest.

C. *Domain Decomposition*

The laser is taken to propagate primarily in the x-direction, and this choice necessitates the use of many more computation cells in the x-direction than in the y-direction. Henceforth, the y-direction shall always taken to be periodic to facilitate the use of fast Fourier transforms (FFT) in solving field equations (see Section D). A one-dimensional parallel decomposition in the y direction has been applied to the two-dimensional computational mesh, as illustrated in Fig. 2 where, as a specific example, the computational mesh consists of 128×128 cells in the x–y (k–l) plane and 16 processors are used. The computational volume is partitioned into N_{pro} equal subdomains where N_{pro} is the number of processors, and each subdomain is assigned to a processor and is henceforth referred to as that processor's private computational volume. In Fig. 2, the thin solid lines denote the boundaries between adjacent computational cells, and the thick solid lines denote the boundaries between the processors' private computational volumes. No parallel decomposition is performed in the x-direction, and each processor holds field data and interpolated density data on cell centers interior to the processor's private computational volume. In addition, each processor also carries a single layer of ghost cells immediately surrounding its private computational volume, as illustrated by the dotted lines in Fig. 2b.

The particles are initially loaded into the processors and are subsequently reassigned among the processors (through the use of interprocessor communications) as the particles' positions evolve, in such a manner which ensures that each particle's position is interior to the private computational volume of the processor to which it is assigned.

D. *Parallel Algorithms for Solving Field Equations*

The spatially discretized versions of Eqs. (15)–(22) are solved by means of a splitting algorithm where the equations are first linearized, and the resulting linearized equations are then solved within a triple-nested modified Newton–Raphson iteration which, upon

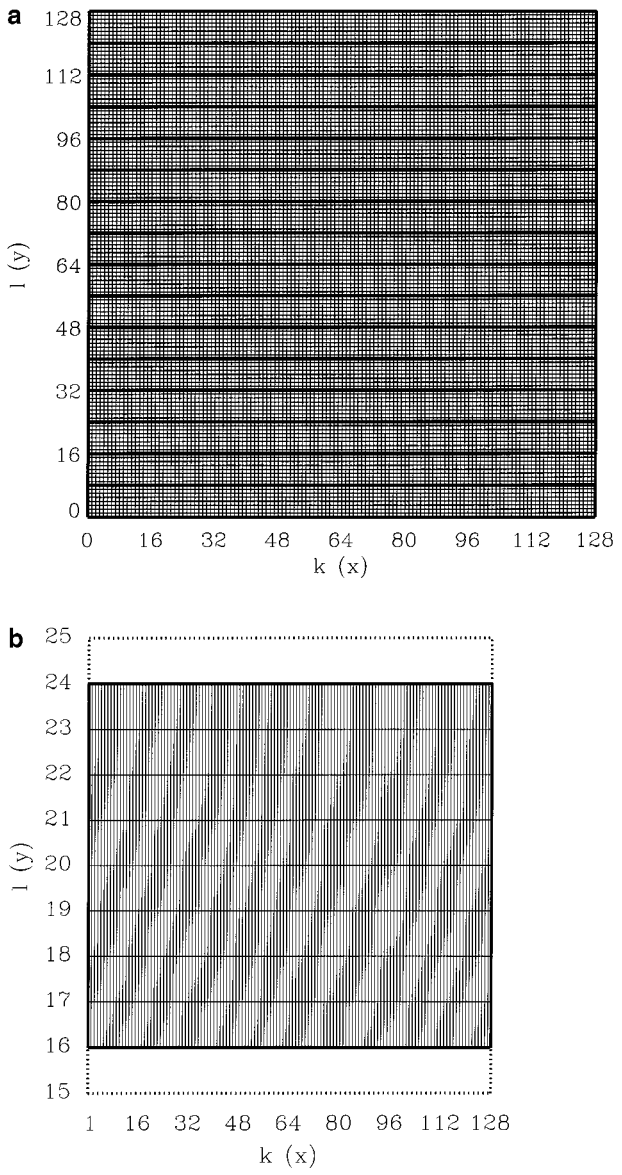

FIG. 2. The one-dimensional decomposition of the two-dimensional volume is illustrated. As a specific example, the computational mesh consists of 128 × 128 cells and 16 processors are used. The thin solid lines denote boundaries between adjacent computational cells, and the thick solid lines denote boundaries between the processors' private computational volumes. Each processor carries a single layer of ghost cells immediately surrounding its private computational volume, as illustrated by the dotted lines.

convergence, yields self-consistent solutions to the original nonlinearly coupled equations, Eqs. (15)–(22). For a more detailed discussion of the splitting algorithm just described, see Ref. [31–33].

The linearized Poisson equation for $\phi_S^{(n)}$ is solved by means of a standard conjugate gradient algorithm with no preconditioning. This method is implemented to run concurrently on all available processors. A more detailed discussion can be found in a previous work [33].

The Poisson equation for $\phi^{(n)}$ is solved by either 2D FFT or a combination of 1D FFT in the y-direction and tridiagonal matrix solves in the x-direction, depending on boundary conditions. For example, if the scalar potential $\phi^{(n)}$ is taken to be 0 at $x = 0$ and $x = L_x$, the Poisson equation can be solved using real-valued FFT in the y-direction and sine FFT in the x-direction. In this case, the ∇^2 operator is transformed to Fourier space symbolically as follows:

$$\nabla^2 \to -k_r^2 \left[\frac{\sin(k_r \delta x/2)}{k_r \delta x/2}\right]^2 - k_s^2 \left[\frac{\sin(k_s \delta y/2)}{k_s \delta y/2}\right]^2,$$
$$k_r \equiv \frac{\pi r}{L_x}, \quad r = 0, 1, \ldots, N_x - 2,$$
$$k_s \equiv \frac{2\pi s}{L_y}, \quad s = 0, 1, \ldots, N_y - 2.$$

The sine FFT in the x direction can be performed concurrently on all available processors, and no interprocessor communication is required. Although the real-valued FFT in the y-direction does require interprocessor communication, it has been implemented to take advantage of any concurrency allowed during the course of an FFT. In particular, assuming that the number of processors N_{pro} is a power of 2, the number of times interprocessor communication is required is only $2 \log_2 N_{pro}$ per FFT in the y-direction. It is found that this is not a significant overhead, as will be shown in Section 6C.

The linearized Schrödinger equations are solved using the pseudo-spectral method which employs complex 1D FFT in the y-direction (the field envelopes are complex-valued) and 1D tridiagonal solves in the x-direction. Here, the ∇ and ∇^2 operators can be written symbolically as follows:

$$\nabla \to \hat{\mathbf{e}}_x \frac{\partial}{\partial x} - i k_s \left[\frac{\sin(k_s \delta y/2)}{k_s \delta y/2}\right] \hat{\mathbf{e}}_y,$$
$$\nabla^2 \to \frac{\partial^2}{\partial x^2} - k_s^2 \left[\frac{\sin(k_s \delta y/2)}{k_s \delta y/2}\right]^2.$$

The nonlinear interaction terms in the Schrödinger equations, e.g., $n_{eS}^{(n-1/2)} \mathbf{a}_0^{(n-1/2)}$, are treated iteratively as known source terms and are computed in configuration space in order to avoid convolutions in Fourier space. The tridiagonal solves in the x direction can be performed concurrently on all available processors, and no interprocessor communication is required.

The macroparticles are scattered evenly across the processors initially. For simulations in which the external electromagnetic field is moderate or weak, the density perturbations are small ($|\delta n_e/n_{e0}| \ll 1$ and $|\delta n_i/n_{i0}| \ll 1$). As a result, the particles do not tend to be spatially bunched, and load balance is well maintained throughout the simulation.

E. *Filtering of Electromagnetic Wave Envelopes*

The pseudo-spectral method for solving the field equations requires that the y-direction is taken to be periodic. Consequently the electromagnetic waves could recycle in that direction. As a result, SRS and SBS may be amplified preferentially in the y-direction since the effective gain region in that direction is essentially infinite. In order to suppress

nonphysical wave recycling, the following filtering scheme is applied to the electromagnetic wave envelopes at each and every computational cycle:

$$h_0(k_y) = \begin{cases} 1 & \text{if } |k_y/k_0| \le 2/F, \\ 0 & \text{otherwise} \end{cases}$$

$$h_1(k_y) = \begin{cases} 1 & \text{if } |k_y/k_1| \le L_y/L_x, \\ 0 & \text{otherwise} \end{cases}$$

$$h_{-1}(k_y) = \begin{cases} 1 & \text{if } |k_y/k_{-1}| \le L_y/L_x, \\ 0 & \text{otherwise} \end{cases}$$

$$k_0 = \frac{\omega_0}{c}\left(1 - \frac{\omega_{pe0}^2}{\omega_0^2}\right)^{1/2},$$

$$k_1 = \frac{\omega_0}{c}\left(1 + 2\frac{\omega_{pe0}}{\omega_0}\right)^{1/2},$$

$$k_{-1} = \frac{\omega_0}{c}\left(1 - 2\frac{\omega_{pe0}}{\omega_0}\right)^{1/2}.$$

Here, F is the f/number of the focusing optics. The electromagnetic wave envelopes $\mathbf{a}_0$, $\mathbf{a}_1$, and $\mathbf{a}_{-1}$ are filtered using h_0, h_1, and h_{-1}, respectively. In all of our simulations, it is observed that the electromagnetic wave spectra are not artificially cut off by the filters presented above; i.e., the important nonzero contributions of the wave spectra are far removed from the cutoff. Consequently, the filters do not introduce adverse numerical effects on the simulation results. Furthermore, it is noted that in all of our simulations, the ratio L_y/L_x (the aspect ratio of the simulation domain) is always chosen to be sufficiently large such that the simulation results are not required to stay within the paraxial limit.

6. RESULTS AND DISCUSSION

The code has been tested in both one and two dimensions. A timing study has been performed, and the results indicate that our code has a high degree of parallel efficiency. Details of this timing study will be presented below, along with results of a two-dimensional test simulation of coexisting SBS, SRS, and LDI.

A. *Numerical Dissipation*

Two of the most prominent types of numerical dissipation will be discussed: (1) electron–ion thermal equilibration and (2) electron heating. Electron–ion thermal equilibration arises from long-range Coulomb collisions between electrons and ions and acts to bring electrons and ions to thermal equilibrium in an energy-conserving manner. While the energy-conserving aspect of this interaction is reflected in the standard explicit PIC algorithm, the equilibration time (due to numerical collisions) is much too short compared to proper physical values. RPIC corrects this deficiency by eliminating the high-frequency response in the ions and thereby eliminating numerical collisions that give rise to electron–ion thermal equilibration. As an illustration, one-dimensional simulations are performed with $T_e/T_i = 30$ using the standard explicit PIC algorithm and ASPEN, and the time histories of the ion and electron temperatures are shown in Fig. 3. In both types of simulations, $\omega_{pe}\delta t = \pi/10$,

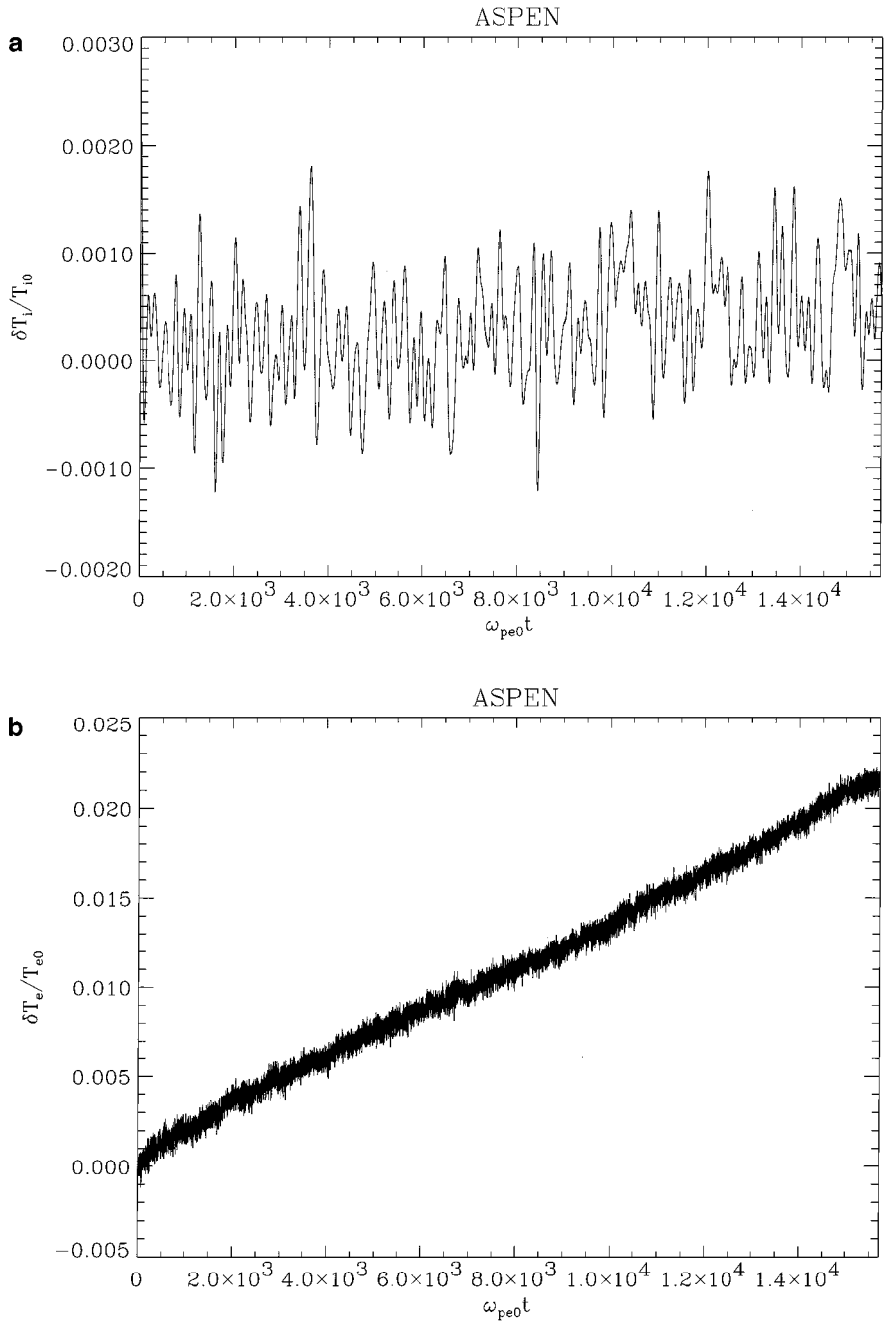

FIG. 3. Time histories of the electron and ion temperatures for periodic, undriven simulations using standard explicit PIC and ASPEN are shown. In both types of simulations, $\omega_{pe}\delta t = \pi/10$, $\delta x/\lambda_{De} = 1$, $L_x/\lambda_{De} = 1024$, $T_e/T_i = 30$, $m_i/m_e = 1836$, and electrons and ions are both represented by 64 macroparticles per computational cell. While there is significant transfer of energy from electrons to ions in the standard PIC method, there is a total absence of energy transfer in ASPEN.

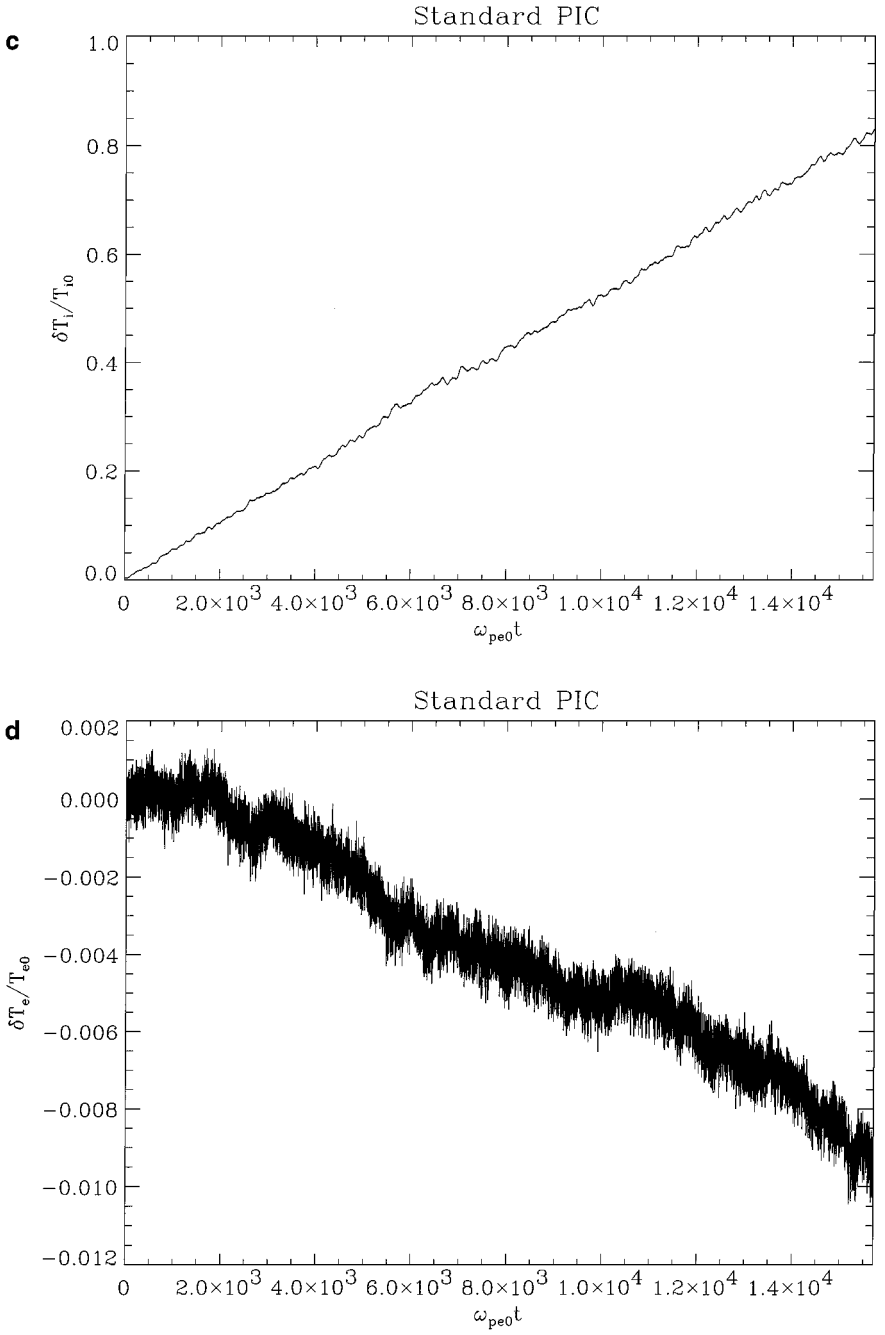

FIG. 3—*Continued*

$\delta x/\lambda_{De} = 1$, $L_x/\lambda_{De} = 1024$, $T_e/T_i = 30$, $m_i/m_e = 1836$, and electrons and ions are both represented by 64 macroparticles per computational cell. The system is undriven with periodic boundary conditions. It is evident that while there is significant energy transfer from electrons to ions with the standard explicit PIC algorithm, there is a total absence of energy transfer with ASPEN.

Numerical dissipation due to finite-grid (aliasing) effects manifests itself in the heating of the electron distribution function even in simulations where there is no external driving field. Such numerical dissipation is nonphysical, does not conserve energy, and is common to both standard explicit PIC and RPIC. The current $\hat{\mathbf{J}}(\mathbf{k}, \omega)$ and the electric field $\hat{\mathbf{E}}(\mathbf{k}, \omega)$ can be expressed via the phenomenological relation $\hat{\mathbf{J}}(\mathbf{k}, \omega) = \nu \hat{\mathbf{E}}(\mathbf{k}, \omega)$, where ν is the electron numerical collision rate. The rate of electron heating is given by Ohmic heating,

$$\frac{d}{dt}\left(\int n_e T_e \, d^3\mathbf{x} \right) = \nu \int \left\langle \frac{|\hat{\mathbf{E}}(\mathbf{k})|^2}{4\pi} \right\rangle d^3\mathbf{k}, \tag{25}$$

where $\langle |\hat{\mathbf{E}}(\mathbf{k})|^2 \rangle$ is given in Eqs. (B.2). As an example, consider the simulations presented in Fig. 3. The rate of electron heating in ASPEN, measured from Fig. 3d, is used in conjunction with Eqs. (25) and (B.2) to calculate the electron numerical collision rate $\nu/\omega_{pe0} \simeq 2.4 \times 10^{-4}$. The dependence of ν on various parameters, e.g., $\delta x/\lambda_{De}$, and various interpolation schemes has been examined in detail by Hockney [37]. In quantitative comparisons of RPIC and quasilinear Zakharov simulations [34], it is important to include ν in the dissipation of Langmuir waves in addition to electron Landau damping because at long wavelengths where electron Landau damping is essentially nonexistent, numerical dissipation is dominant. In the specific example given in Fig. 3, numerical dissipation dominates over electron Landau damping for $k\lambda_{De} < .213$.

B. *Two-Dimensional Simulation of SBS, SRS, and LDI*

The simulation is performed in a rectangular simulation box with $L_y = 12$ μm and $L_x = 25$ μm. The boundary conditions are periodic in the y-direction, and aperiodic in the x-direction. The electromagnetic pump wave enters the simulation domain at $x = 0$ and leaves the simulation domain at $x = L_x$. The corresponding boundary conditions for the scalar and vector potentials are

$$\begin{aligned}
\phi(0, y, t) &= \phi(L_x, y, t) = 0, \\
\phi_S(0, y, t) &= \phi_S(L_x, y, t) = 0, \\
\hat{\mathbf{e}}_x \cdot \nabla \mathbf{a}_0(0, y, t) &= ik_0(2\mathbf{a}_{in}(y) - \mathbf{a}_0(0, y, t)), \\
\hat{\mathbf{e}}_x \cdot \nabla \mathbf{a}_0(L_x, y, t) &= ik_0 \mathbf{a}_0(L_x, y, t), \\
\hat{\mathbf{e}}_x \cdot \nabla \mathbf{a}_1(0, y, t) &= -ik_1 \mathbf{a}_1(0, y, t), \\
\hat{\mathbf{e}}_x \cdot \nabla \mathbf{a}_1(L_x, y, t) &= ik_1 \mathbf{a}_1(L_x, y, t), \\
\hat{\mathbf{e}}_x \cdot \nabla \mathbf{a}_{-1}(0, y, t) &= -ik_{-1} \mathbf{a}_{-1}(0, y, t), \\
\hat{\mathbf{e}}_x \cdot \nabla \mathbf{a}_{-1}(L_x, y, t) &= ik_{-1} \mathbf{a}_{-1}(L_x, y, t).
\end{aligned}$$

Here, $\mathbf{a}_{in}(y)$ is a specified function and corresponds to the incident electromagnetic wave at $x = 0$. $\mathbf{a}_{in}$ is related to the incident laser intensity I as follows:

$$|\mathbf{a}_{in}(y)|^2 = \left(\frac{8\pi}{c\omega_0^2} \right) I(y).$$

For the particular simulation under consideration, $\mathbf{a}_{in}$ is specified as follows:

$$\mathbf{a}_{in}(y) = \left(\frac{8\pi I_0}{c\omega_0^2}\right)^{1/2}\left(\frac{2f}{k_0\sigma_0}\right)\exp\left[-\frac{1}{4\sigma_0^2}\left(y-\frac{L_y}{2}\right)^2\right],$$

$$\sigma_0^2 = \left(\frac{2f}{k_0}\right)^2 - i\left(\frac{L_x}{4k_0}\right).$$

Here, I_0 is the diffraction-limited intensity of the laser and is taken to be 6.7×10^{15} W/cm^2. ω_0, the frequency of the incident laser, is taken to be 5.37×10^{15} Hz and corresponds to a frequency-tripled Nd–glass laser with vacuum wavelength $\lambda_v = 0.351$ μm. The f/number of the focusing optics, defined to be the ratio of the focal length of the optical lens to its diameter, is taken to be 4.0. It is noted here that with the above boundary conditions for $\mathbf{a}_m$ ($m=-1, 0, 1$), electromagnetic noise is not injected into the simulation domain. Consequently, parametric instabilities such as SBS and SRS develop from noise in the electron and ion density. It is noted here that the electromagnetic field is taken to be polarized in the z-direction (the ignorable coordinate), and χ_m and ξ_m can therefore be set identically to 0 at all times.

Initially, the plasma is spatially uniform and stationary and the initial condition for $\mathbf{a}_m$ is

$$\mathbf{a}_0(x,y,0) = \left(\frac{8\pi I_0}{c\omega_0^2}\right)^{1/2}\left(\frac{2f}{k_0\sigma(x)}\right)\exp\left[-\frac{1}{4\sigma^2(x)}\left(y-\frac{L_y}{2}\right)^2\right],$$

$$\sigma^2(x) = \left(\frac{2f}{k_0}\right)^2 + i\left(\frac{x-L_x/2}{4k_0}\right),$$

$$\mathbf{a}_1(x,y,0) = 0,$$

$$\mathbf{a}_{-1}(x,y,0) = 0.$$

The plasma consists of protons and electrons with $n_i = n_e = 8.9\times10^{20}$ cm^{-3}, $T_e = 1.6$ keV, and $T_i = 0.1$ keV. The ratio of specific heats γ is taken to be 1. The simulation box has 4096×256 (1 million) computational cells, each particle species is represented by 64 particles per computational cell (a total of 128 million particles), and the time step is taken to be $\omega_{pe0}\delta t = \pi/10$. For this particular simulation, SBS, SRS, and LDI are observed to occur simultaneously. The simulation consists of 36,000 computational cycles and corresponds to a physical time of 7 ps.

Figure 4 shows the time histories of the SBS and SRS reflectivities. While SRS has saturated, SBS is still undergoing exponential growth. Figure 5 is a color-coded contour plot of the time-averaged 2D (k_x-k_y) LW spectrum, accompanied by the k_y-averaged LW spectrum. The LW spectrum is seen to consist of two LWs whose locations in k-space are predicted accurately by wave-matching conditions. First, linear wave-matching conditions for SRS require that

$$k_{\mathrm{LW1}}\lambda_{De} = \left(\frac{v_{the}}{c}\right)\left(\frac{\omega_0}{\omega_{pe0}}\right)\left[\left(1-\frac{\omega_{pe0}^2}{\omega_0^2}\right)^{1/2} + \left(1-2\frac{\omega_{pe0}}{\omega_0}\right)^{1/2}\right],$$

where k_{LW1} is the wavenumber of the LWs generated by SRS. For the simulation under discussion, $k_{\mathrm{LW1}}\lambda_{De} \approx 0.277$. This SRS-generated LW undergoes the LDI parametric process

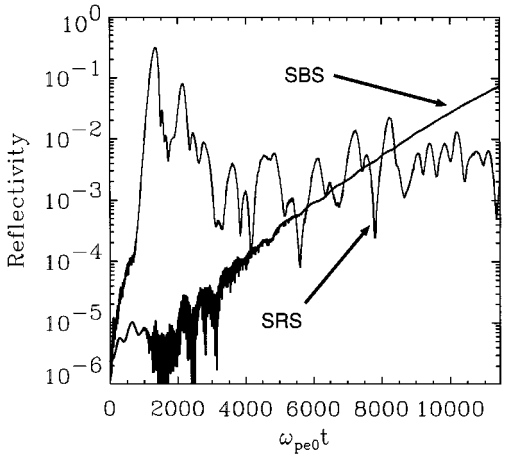

FIG. 4. Time histories of the SBS and SRS reflectivities for a two-dimensional simulation are shown. The laser is Gaussian diffraction-limited with $f/4$, $I_0 = 6.7 \times 10^{15}$ W/cm^2, and $\lambda_0 = 0.351\,\mu$m. The plasma consists of protons and electrons with $n_i = n_e = 8.9 \times 10^{20}$ cm^{-3}, $T_e = 1.6$ keV, and $T_i = 0.1$ keV. The ratio of specific heats γ is taken to be 1. The simulation box has 4096×256 (1 million) computational cells, and each particle species is represented by 64 particles per computational cell (a total of 128 million particles). For this simulation, $\omega_{pe0}\delta t = \pi/10$.

in which it decays into another LW and an IAW whose wavenumbers are given by linear wave-matching conditions,

$$k_{\mathrm{LW2}}\lambda_{De} = -k_{\mathrm{LW1}}\lambda_{De} + \frac{2}{3}\left(\frac{c_s}{v_{the}}\right),$$
$$k_{\mathrm{IAW2}}\lambda_{De} = k_{\mathrm{LW1}}\lambda_{De} - k_{\mathrm{LW2}}\lambda_{De},$$

where c_s and v_{the} are the ion acoustic and electron thermal speeds, respectively. Here, c_s is computed from the kinetic linear dispersion relation for IAWs to be $c_s/c \approx 2.63 \times 10^{-3}$. For the simulation under discussion, $k_{\mathrm{LW2}}\lambda_{De} \approx -0.246$ and $k_{\mathrm{IAW2}}\lambda_{De} \approx 0.523$. Figure 6 is a color-coded contour plot of the time-averaged 2D (k_x-k_y) IAW spectrum, accompanied by the k_y-averaged IAW spectrum. The IAW spectrum is seen to consist of (a) the SBS-generated IAW and its second and third harmonics, (b) the LDI-generated IAW at $k_{\mathrm{IAW2}} \approx 0.523$, (c) the beat waves resulting from the interaction between the SBS-generated IAW and the LDI-generated IAW, and (d) the density profile modification due to the ponderomotive force. Linear wave-matching conditions require that the SBS-generated IAW be located at

$$k_{\mathrm{IAW3}}\lambda_{De} = 2\left(\frac{v_{the}}{c}\right)\left(\frac{\omega_0}{\omega_{pe0}}\right)\left[\left(1 - \frac{\omega_{pe0}^2}{\omega_0^2}\right)^{1/2} - \frac{c_s}{c}\right].$$

For the simulation under consideration, $k_{\mathrm{IAW3}}\lambda_{De} \approx 0.337$. The second and third harmonics of this SBS-generated IAW must then be located at $k_{\mathrm{IAW4}}\lambda_{De} \approx 0.674$ and $k_{\mathrm{IAW5}}\lambda_{De} \approx 1.01$. The pair of IAWs which result from the beating between the SBS-generated and LDI-generated IAWs at k_{IAW3} and k_{IAW2} are expected to be located at $k_{\mathrm{IAW7}}\lambda_{De} \approx 0.860$ and $k_{\mathrm{IAW9}}\lambda_{De} \approx 0.186$.

Figure 7 is a color-coded contour plot of the 2D (x-y) ion-density perturbation, accompanied by the x-averaged and y-averaged ion-density perturbation. Figure 7 indicates a density

TABLE Ia

No. of processors	Grid size	CPU seconds	Speed up
2	4096×256	1183	
4	4096×256	642.4	1.84
8	4096×256	339.7	1.89
16	4096×256	158.7	2.14
32	4096×256	78.86	2.01
64	4096×256	38.88	2.03

perturbation of about 4% due to the ponderomotive force. The short-wavelength density perturbations in the y-averaged ion density are primarily due to SBS. Figure 8 is the distribution of electrons leaving (a) the left boundary and (b) the right boundary. These distributions indicate the asymmetric development of hot electron tails, which is consistent with the fact that the primary LW (due to SRS) is stronger than the secondary LW (due to LDI).

It is noted here that even in a single laser hot spot such as the one shown in this section, an abundance of parametric instabilities whose daughter waves exist on highly disparate time scales can coexist and interact in a complex manner. The interaction between these instabilities and the role of nonlinear and quasilinear kinetic effects on these instabilities are not well understood. We plan to use ASPEN to address these issues, and the results will be reported in a future publication.

C. *Timing Studies*

The parallel efficiency of our code ASPEN depends primarily on two sets of operations: (1) the FFT algorithm, which is used extensively to solve for the field envelopes as discussed previously, and (2) the particle pusher and interpolation algorithm. As a result, two sets of timing studies were performed in order to assess the parallel efficiency of the FFT and the overall parallel efficiency of ASPEN. The results to be presented below are particular to the Los Alamos ASCI computer, which consists of Silicon Graphics' 250 MHz R10000 processors.

A computational mesh of 4096×256 is employed in our test of the FFT algorithm. Here, 500 complex-valued 2D FFTs are performed, and the CPU time required to do the task is recorded as a function of number of processors and is shown in Table Ia. The average speedup x, where $x^5 \equiv$ CPU time required by 64 processors/CPU time required by 2 processors, is calculated from Table Ia to be 1.98, indicating that the FFT algorithm performs with near-perfect parallel efficiency in this regime. Next, a similar test is performed with a computational mesh of 4096×64, and the results are summarized in Table Ib. The average speedup is calculated from Table Ib to be 1.80.

TABLE Ib

No. of processors	Grid size	CPU seconds	Speed up
2	4096×64	186.	
4	4096×64	98.2	1.89
8	4096×64	50.4	1.95
16	4096×64	27.5	1.83
32	4096×64	17.4	1.58
64	4096×64	9.73	1.79

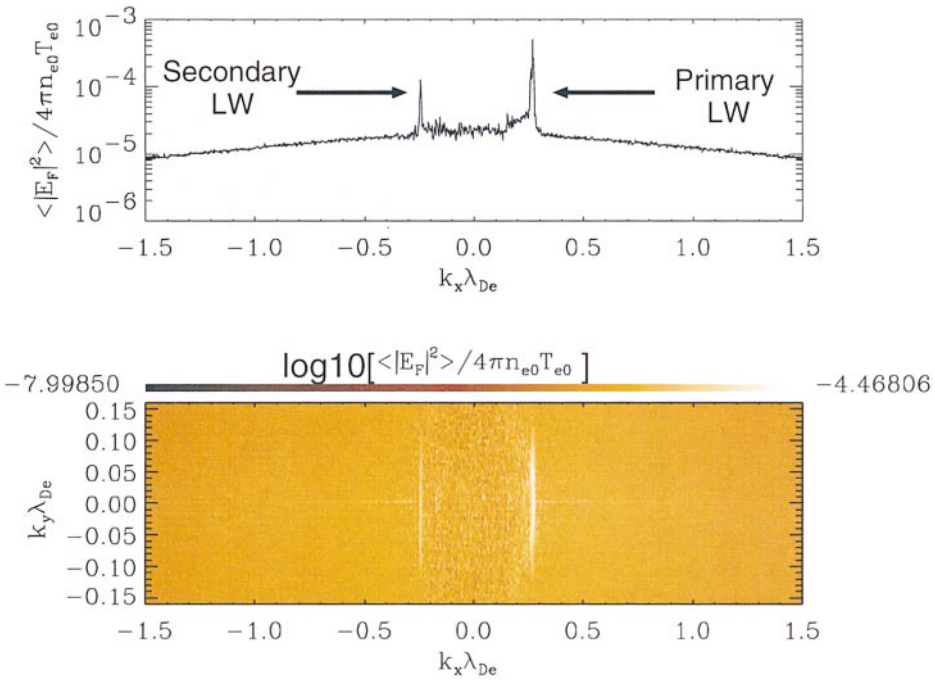

FIG. 5. Color-coded contour plots of the Langmuir wave energy spectrum corresponding to the case described in Fig. 4. The spectrum has been averaged over the entire duration of the simulation ($\omega_{pe0}T = 1.13 \times 10^4$, corresponding to a physical time of 7 ps). For clarity, only a small part of the 2D **k**-space is shown. The top panel is the k_y-averaged Langmuir wave spectrum. The primary Langmuir wave is driven by SRS, and the secondary Langmuir wave is, in turn, driven by the primary Langmuir wave.

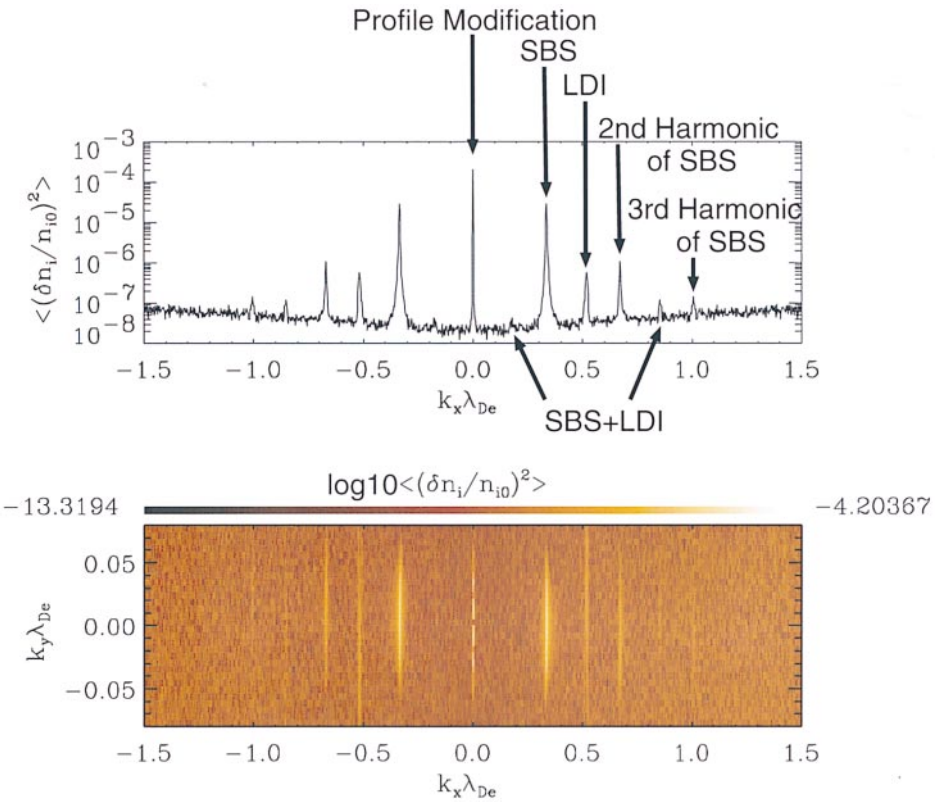

FIG. 6. Color-coded contour plots of the ion acoustic wave energy spectrum corresponding to the case described in Fig. 4. The spectrum has been averaged over the entire duration of the simulation ($\omega_{pe0}T = 1.13 \times 10^4$, corresponding to a physical time of 7ps). For clarity, only a small part of the 2D **k**-space is shown. The top panel is the k_y-averaged ion acoustic wave spectrum. The SBS-generated ion acoustic wave and its second and third harmonics and the LDI-generated ion acoustic wave are seen to coexist and interact via nonlinear beating of the waves.

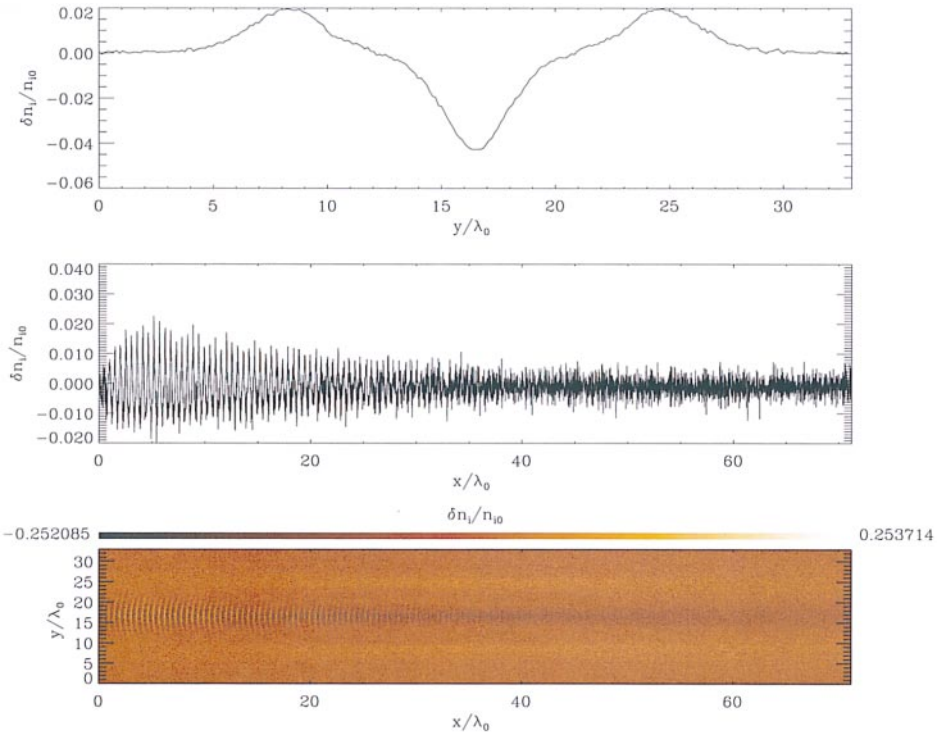

FIG. 7. Color-coded contour plots of the ion density perturbation corresponding to the case described in Fig. 4. The ion density perturbation shown here is a snapshot at $\omega_{pe0}t = 1.13 \times 10^4$. Also shown are the x-averaged and y-averaged ion density perturbations. The ion density perturbation due to the ponderomotive force is about 4%, and the ion density perturbation due to SBS and LDI is about 2%.

Second, in order to assess the overall parallel efficiency of ASPEN, a test simulation is performed in which the computational mesh consists of 1024×256 cells and the ion and electrons are represented by a total of 256 particles/cell. The simulation is performed, and the CPU time required to execute 10 time cycles is recorded and is summarized in Table II. The average speedup, defined previously, is computed from Table II to be 1.91 and indicates that overall, ASPEN has a high degree of parallel efficiency. In fact, this type of performance is similar to that reported for HERCULES [32], a three-dimensional massively parallel hybrid PIC code designed specifically for low-frequency parametric interactions in laser-produced plasmas, in which a speedup factor of 1.9 was obtained for a CRAY T3D with 512 processors.

TABLE II

No. of processors	Grid size	No. of particles/cell	CPU seconds	Speed up
2	1024×256	256	640	
4	1024×256	256	320	2.00
8	1024×256	256	158	2.02
16	1024×256	256	81.2	1.95
32	1024×256	256	45.0	1.81
64	1024×256	256	25.0	1.80

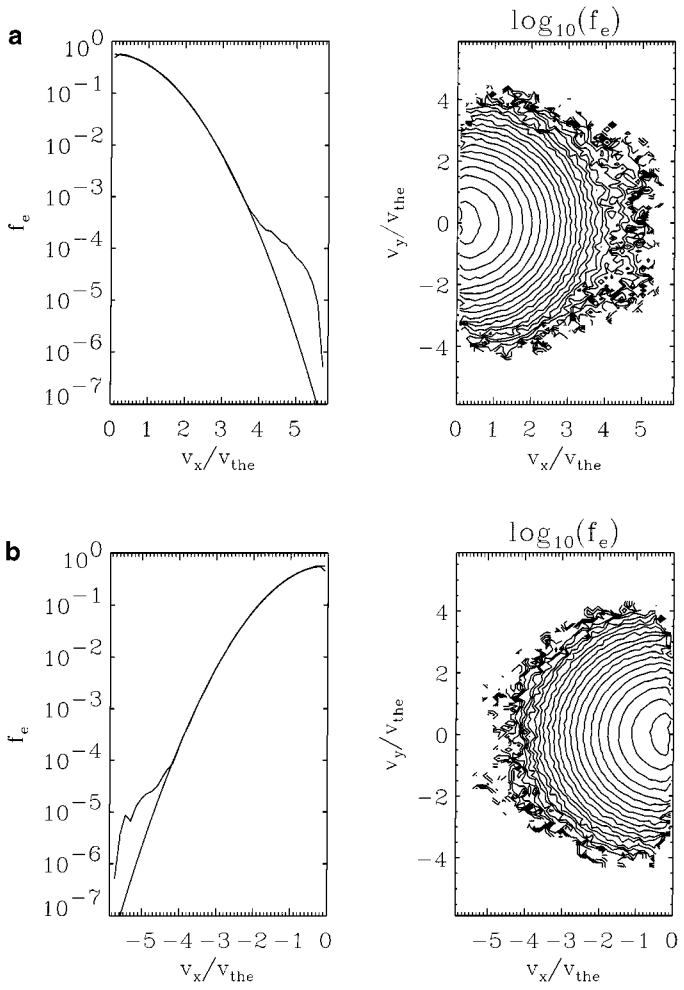

FIG. 8. Contour plots of the electron distribution function corresponding to the case described in Fig. 4: (a) electrons that leave the boundary located at $x = L_x$ (electrons that move in the direction of the primary Langmuir wave), and (b) electrons that leave the boundary located at $x = 0$ (electrons that move in the direction of the secondary Langmuir wave). The asymmetry in the hot electron tails is due to the fact that the primary Langmuir wave is stronger than the secondary Langmuir wave.

7. SUMMARY AND CONCLUSIONS

In this report, a massively parallel two-dimensional RPIC code, implemented on the Los Alamos ASCI parallel computer, appropriate for modeling parametric instabilities in laser-produced plasmas with both low-frequency and high-frequency daughter waves is presented. The physics model contained therein is an extension of an earlier model in which only low-frequency parametric instabilities are treated [33]. The RPIC model consists of three coupled nonlinear Schrödinger-like equations for the vector potentials, Poisson equations for the scalar potentials, an exactly integrable electron momentum equation, and the equations of motion for the finite-size electron and ion particles. The Schrödinger equations are solved using the standard pseudo-spectral method. The Poisson equation for the instantaneous electrostatic potential is solved using a combination of tridiagonal matrix solver and FFT.

The low-frequency electrostatic potential is solved using the standard conjugate gradient algorithm without preconditioning.

Temporal mean-square noise spectra have been calculated analytically and compared with simulation results. The availability of these noise spectra facilitate quantitative comparisons between the RPIC model and the Zakharov model augmented with quasilinear evolution of the spatially averaged electron distribution function [34]. Two-dimensional simulations of SRS, SBS, and LDI and the interaction of these instabilities have been performed, and the results of one such simulation was presented. The results show a complex interaction between these instabilities, which occur on very disparate time scales. We plan to utilize ASPEN to study the interaction between these instabilities, a subject of intense interest to the ICF community at present.

In our test simulations for which there are 64 particles/species/cell, it was found that with 128 processors, the code requires about 0.08 μs/particle/time step. The timing results indicate that code has a high degree of efficiency, evidenced by the fact that the CPU time required is reduced by a factor of about 1.9 on average whenever the number of processors is doubled.

APPENDIX A

Derivation of Electron Equation of State

Summing Eqs. (2) over the electron distribution, one obtains the following electron fluid equation,

$$m_e\left(\frac{\partial \mathbf{U}_e}{\partial t}+\mathbf{U}_e\cdot\nabla\mathbf{U}_e\right)=e\nabla\phi-\frac{e^2}{4m_ec^2}\nabla\left(\mathbf{a}_m\cdot\mathbf{a}_l^*\mathrm{e}^{-i(m-l)\omega_{pe0}t}\right)-\frac{1}{n_e}\nabla p_e$$
$$\mathbf{U}_e\approx\mathbf{U}_{eS}+\frac{1}{2}\left(\mathbf{U}_{eF}\mathrm{e}^{-i\omega_{pe0}t}+\mathbf{U}_{eF}^*\mathrm{e}^{i\omega_{pe0}t}\right), \tag{A.1}$$

where $\mathbf{U}_e$ and p_e are the longitudinal electron fluid velocity (defined in Section 3) and electron pressure, respectively. The high-frequency and low-frequency parts of Eqs. (A.1) describe the electron response due to ion acoustic and Langmuir waves, respectively. Neglecting the small contributions of both the electron pressure and the advection term, and assuming $|\partial\mathbf{U}_{eF}/\partial t|\ll\omega_{pe0}|\mathbf{U}_{eF}|$, $\mathbf{U}_{eF}$ is obtained from the high-frequency component of Eqs. (A.1):

$$\mathbf{U}_{eF}\approx-\frac{1}{im_e\omega_{pe0}}\nabla\left(e\phi_F-\frac{e^2}{2m_ec^2}(\mathbf{a}_0\cdot\mathbf{a}_{-1}^*+\mathbf{a}_0^*\cdot\mathbf{a}_1)\right). \tag{A.2}$$

Substituting Eq. (A.2) into Eqs. (A.1) and neglecting the low-frequency electron inertia, the low-frequency component of Eqs. (A.1) can be recast as follows:

$$\frac{1}{4m_e\omega_{pe0}^2}\nabla\left|\nabla\left[e\phi_F-\frac{e^2}{2m_ec^2}(\mathbf{a}_0\cdot\mathbf{a}_{-1}^*+\mathbf{a}_0^*\cdot\mathbf{a}_1)\right]\right|^2$$
$$=e\nabla\phi_S-\frac{1}{n_{eS}}\nabla p_{eS}-\frac{e^2}{4m_ec^2}\nabla(\mathbf{a}_m\cdot\mathbf{a}_m^*). \tag{A.3}$$

For moderate incident electromagnetic field intensities, the bulk electron distribution is not expected to be perturbed significantly, and the low-frequency electron pressure can be assumed to obey an adiabatic equation of state with an arbitrary ratio of specific heats γ. Following the approach outlined previously by Vu [31–33], Eq. (A.3) can be integrated to obtain the electron equation of state, and the results are shown in Eqs. (8) and (9).

APPENDIX B

Noise Spectra

In the absence of external fields, the linearized Vlasov equations for a two-component (electrons and ions) plasma described by Eqs. (2)–(10) are as follows,

$$\frac{\partial \delta f_e}{\partial t} + \mathbf{u}\cdot\nabla\delta f_e + \frac{\partial}{\partial \mathbf{u}} \cdot\left[\frac{e}{m_e}\sum_{p\in e} q_p S(\mathbf{x}-\mathbf{x}_p)\delta(\mathbf{u}-\mathbf{u}_{p0})\frac{\partial}{\partial \mathbf{x}_p}\left[\int \phi(\mathbf{x}')S(\mathbf{x}'-\mathbf{x}_p)\,d^3\mathbf{x}'\right]\right] = 0,$$

$$\frac{\partial \delta f_i}{\partial t} + \mathbf{u}\cdot\nabla\delta f_i - \frac{\partial}{\partial \mathbf{u}} \cdot\left[\frac{eZ}{m_i}\sum_{p\in i} q_p\, S(\mathbf{x}-\mathbf{x}_p)\delta(\mathbf{u}-\mathbf{u}_{p0})\frac{\partial}{\partial \mathbf{x}_p}\left[\int \phi_S(\mathbf{x}')S(\mathbf{x}'-\mathbf{x}_p)\,d^3\mathbf{x}'\right]\right] = 0,$$

$$\begin{aligned}
\mathbf{x}_p &\equiv \mathbf{x}_{p0} + \mathbf{u}_{p0}t,\\
\nabla^2\phi &= 4\pi e(n_{e1} - Zn_{i1}),\\
\nabla^2\phi_S &= 4\pi e\left(n_{e0}\,\frac{e\phi_S}{T_e} - Zn_{i1}\right),\\
n_{e1}(\mathbf{x},t) &\equiv \int \delta f_e(\mathbf{x},\mathbf{u},t)\,d^3\mathbf{u} + \sum_{p\in e} q_p S(\mathbf{x}-\mathbf{x}_p) + en_{e0},\\
n_{i1}(\mathbf{x},t) &\equiv \int \delta f_i(\mathbf{x},\mathbf{u},t)\,d^3\mathbf{u} + \sum_{p\in i} q_p S(\mathbf{x}-\mathbf{x}_p) - en_{e0},
\end{aligned}$$

where $S(\mathbf{x})$ is the particle interpolation function whose Fourier transform is $\hat{S}(\mathbf{k})$, n_{e0} is the uniform background electron number density, and δf_e and δf_i are the perturbations from straight-line particle orbits.

Because the time step of the simulation is usually small, i.e., $\omega_{pe0}\delta t \ll 1$, the effects of time discretization can be neglected. Also, because a staggered mesh is employed (see Section 5), the operators ∇ and ∇^2 can be written symbolically as follows:

$$\begin{aligned}
\nabla &= i\hat{\mathbf{k}},\\
\nabla^2 &= -\hat{k}^2,\\
\hat{\mathbf{k}} &\equiv k_x\left[\frac{\sin(k_x\delta x/2)}{k_x\delta x/2}\right]\mathbf{e}_x + k_y\left[\frac{\sin(k_y\delta y/2)}{k_y\delta y/2}\right]\mathbf{e}_y.
\end{aligned}$$

Solving the above equations for δf_e and δf_i in Fourier space, assuming Maxwellian electrons and ions of temperature T_{e0} and T_{i0}, respectively, and integrating the results over velocities, one obtains

$$\begin{aligned}
\frac{\hat{n}_{e1}(\mathbf{k},\omega)}{n_{e0}} &= \frac{\hat{S}(\mathbf{k})}{N_e}\frac{1}{1+\chi_e(\mathbf{k},\omega)}\sum_{p\in e} e^{-i\mathbf{k}\cdot\mathbf{x}_{p0}}\delta(\omega-\mathbf{k}\cdot\mathbf{u}_{p0}) \\
&\quad + \frac{\hat{S}(\mathbf{k})}{N_i}\frac{\chi_e(\mathbf{k},\omega)}{\bar{\epsilon}(\mathbf{k},\omega)}\frac{1+\bar{\chi}_e(\mathbf{k})}{1+\chi_e(\mathbf{k},\omega)}\sum_{p\in i} e^{-i\mathbf{k}\cdot\mathbf{x}_{p0}}\delta(\omega-\mathbf{k}\cdot\mathbf{u}_{p0}), \\
\frac{\hat{n}_{i1}(\mathbf{k},\omega)}{n_{i0}} &= \frac{\hat{S}(\mathbf{k})}{N_i}\frac{1+\bar{\chi}_e(\mathbf{k})}{\bar{\epsilon}(\mathbf{k},\omega)}\sum_{p\in i} e^{-i\mathbf{k}\cdot\mathbf{x}_{p0}}\delta(\omega-\mathbf{k}\cdot\mathbf{u}_{p0}), \qquad \text{(B.1)} \\
\hat{\mathbf{E}}(\mathbf{k},\omega) &= -\frac{i\hat{\mathbf{k}}}{\hat{k}^2}\frac{4\pi e n_{e0}\hat{S}(\mathbf{k})}{N_e}\frac{1}{1+\chi_e(\mathbf{k},\omega)}\sum_{p\in e} e^{-i\mathbf{k}\cdot\mathbf{x}_{p0}}\delta(\omega-\mathbf{k}\cdot\mathbf{u}_{p0}) \\
&\quad + \frac{i\hat{\mathbf{k}}}{\hat{k}^2}\frac{4\pi e n_{e0}\hat{S}(\mathbf{k})}{N_i}\frac{1}{\bar{\epsilon}(\mathbf{k},\omega)}\frac{1+\bar{\chi}_e(\mathbf{k})}{1+\chi_e(\mathbf{k},\omega)}\sum_{p\in i} e^{-i\mathbf{k}\cdot\mathbf{x}_{p0}}\delta(\omega-\mathbf{k}\cdot\mathbf{u}_{p0}).
\end{aligned}$$

The susceptibilities and dielectric response are defined as follows:

$$\begin{aligned}
\chi_e(\mathbf{k},\omega) &\equiv -\frac{1}{2}\left(\frac{k_{De}}{\hat{k}}\right)^2\hat{S}^2(\mathbf{k})Z'\left(\frac{\omega}{\sqrt{2}kv_{the}}\right), \\
\bar{\chi}_e(\mathbf{k}) &\equiv \left(\frac{k_{De}}{\hat{k}}\right)^2, \\
\chi_i(\mathbf{k},\omega) &\equiv -\frac{1}{2}\left(\frac{k_{Di}}{\hat{k}}\right)^2\hat{S}^2(\mathbf{k})Z'\left(\frac{\omega}{\sqrt{2}kv_{thi}}\right), \\
\bar{\epsilon}(\mathbf{k},\omega) &\equiv 1+\bar{\chi}_e(\mathbf{k})+\chi_i(\mathbf{k},\omega), \\
v_{the}^2 &\equiv \frac{T_{e0}}{m_e}, \quad v_{thi}^2 \equiv \frac{T_{i0}}{m_i}, \\
\omega_{pe0}^2 &\equiv \frac{4\pi e^2 n_{e0}}{m_e}, \quad \omega_{pi0}^2 \equiv \frac{4\pi Z e^2 n_{e0}}{m_i}, \\
k_{De}^2 &\equiv \frac{\omega_{pe0}^2}{v_{the}^2}, \quad k_{Di}^2 \equiv \frac{\omega_{pi0}^2}{v_{thi}^2}.
\end{aligned}$$

Here, it has been assumed that the electrons and ions in the simulation domain are represented by N_e and N_i equally weighted macroparticles, respectively. $Z(\xi)$ is the plasma dispersion function and is defined as follows:

$$Z(\xi) \equiv \frac{1}{\sqrt{\pi}}\int_{-\infty}^{\infty}\frac{e^{-z^2}}{z-\xi}\,dz, \quad \text{Im}\,\xi > 0.$$

Using Parseval's theorem and the Kramers–Kronig relations, the temporal mean-square

density fluctuations are evaluated analytically from Eqs. (B.1):

$$\left\langle \left| \frac{\hat{n}_{e1}(\mathbf{k})}{n_{e0}} \right|^2 \right\rangle = \frac{1}{N_e} \sum_g \frac{S^2(\mathbf{k}-\mathbf{k}_g)}{1+\chi_e(\mathbf{k}-\mathbf{k}_g,0)} + \frac{1}{N_i} \sum_g \frac{S^2(\mathbf{k}-\mathbf{k}_g)\chi_e^2(\mathbf{k}-\mathbf{k}_g,0)[1+\bar{\chi}_e(\mathbf{k}-\mathbf{k}_g)]}{\bar{\epsilon}(\mathbf{k}-\mathbf{k}_g,0)[1+\chi_e(\mathbf{k}-\mathbf{k}_g,0)]^2},$$

$$\left\langle \left| \frac{\hat{n}_{i1}(\mathbf{k})}{n_{i0}} \right|^2 \right\rangle = \frac{1}{N_i} \sum_g \frac{S^2(\mathbf{k}-\mathbf{k}_g)[1+\bar{\chi}_e(\mathbf{k}-\mathbf{k}_g)]}{\bar{\epsilon}(\mathbf{k}-\mathbf{k}_g,0)}, \tag{B.2}$$

$$\left\langle \frac{|\hat{\mathbf{E}}(\mathbf{k})|^2}{4\pi n_{e0} T_{e0}} \right\rangle = \frac{1}{N_e} \sum_g \frac{\chi_e(\mathbf{k}-\mathbf{k}_g,0)}{1+\chi_e(\mathbf{k}-\mathbf{k}_g,0)} + \frac{1}{N_i} \sum_g \frac{\chi_e(\mathbf{k}-\mathbf{k}_g,0)[1+\bar{\chi}_e(\mathbf{k}-\mathbf{k}_g)]}{\bar{\epsilon}(\mathbf{k}-\mathbf{k}_g,0)[1+\chi_e(\mathbf{k}-\mathbf{k}_g,0)]^2},$$

$$\mathbf{k}_g = \frac{2\pi p}{\delta x}\hat{\mathbf{e}}_x + \frac{2\pi q}{\delta y}\hat{\mathbf{e}}_y \quad p, q = \text{integer}.$$

Here, $|k_x| \le \pi/\delta x$, $|k_y| \le \pi/\delta y$, and $\sum_g$ represents the sum over all Brillouin zones. In effect, $\sum_g$ accounts for aliasing effects in $\mathbf{k}$-space. It is noted here that in the limit where $|k_x \delta x| \ll 1$ and $|k_y \delta y| \ll 1$, Eqs. (B.2) yield the standard mean-square density fluctuations in a thermal plasma. Using Eqs. (7) and (B.1), the temporal mean-square fluctuations of the density and potential envelopes are evaluated explicitly:

$$\left\langle \left| \frac{\hat{n}_{e1S}(\mathbf{k})}{n_{e0}} \right|^2 \right\rangle = \frac{1}{N_i} \sum_g \frac{S^2(\mathbf{k}-\mathbf{k}_g)\bar{\chi}_e^2(\mathbf{k}-\mathbf{k}_g)}{\bar{\epsilon}(\mathbf{k}-\mathbf{k}_g,0)[1+\bar{\chi}_e(\mathbf{k}-\mathbf{k}_g)]},$$

$$\left\langle \left| \frac{\hat{n}_{e1F}(\mathbf{k})}{n_{e0}} \right|^2 \right\rangle = \sum_g \frac{S^2(\mathbf{k}-\mathbf{k}_g)}{N_e} \left[\frac{1}{1+\chi_e(\mathbf{k}-\mathbf{k}_g,0)} + \frac{|\mathbf{k}-\mathbf{k}_g|^2}{k_{De}^2} \right] + \frac{1}{N_i} \sum_g \frac{S^2(\mathbf{k}-\mathbf{k}_g)[1-S^2(\mathbf{k}-\mathbf{k}_g)]^2 \bar{\chi}_e^2(\mathbf{k}-\mathbf{k}_g)}{\bar{\epsilon}(\mathbf{k}-\mathbf{k}_g,0)[1+\chi_e(\mathbf{k}-\mathbf{k}_g,0)]^2[1+\bar{\chi}_e(\mathbf{k}-\mathbf{k}_g)]},$$

$$\left\langle \left| \frac{e\hat{\phi}_S(\mathbf{k})}{T_{e0}} \right|^2 \right\rangle = \left\langle \left| \frac{\hat{n}_{e1S}(\mathbf{k})}{n_{e0}} \right|^2 \right\rangle, \tag{B.3}$$

$$\left\langle \left| \frac{e\hat{\phi}_F(\mathbf{k})}{T_{e0}} \right|^2 \right\rangle = \sum_g \frac{S^2(\mathbf{k}-\mathbf{k}_g)}{N_e} \left[\frac{1}{1+\chi_e(\mathbf{k}-\mathbf{k}_g,0)} + \frac{|\mathbf{k}-\mathbf{k}_g|^2}{k_{De}^2} \right] \bar{\chi}_e^2(\mathbf{k}-\mathbf{k}_g) + \frac{1}{N_i} \sum_g \frac{S^2(\mathbf{k}-\mathbf{k}_g)\left[1-S^2(\mathbf{k}-\mathbf{k}_g)\right]^2 \bar{\chi}_e^4(\mathbf{k}-\mathbf{k}_g)}{\bar{\epsilon}(\mathbf{k}-\mathbf{k}_g,0)[1+\chi_e(\mathbf{k}-\mathbf{k}_g,0)]^2[1+\bar{\chi}_e(\mathbf{k}-\mathbf{k}_g)]}.$$

ACKNOWLEDGMENT

This work was performed under the auspices of the United States Department of Energy and is supported by the Inertial Confinement Fusion Theory and Design Program at Los Alamos.

REFERENCES

1. W. L. Kruer, *The Physics of Laser Plasma Interactions* (Addison-Wesley, New York, 1988).
2. J. C. Fernandez, B. S. Bauer, J. A. Cobble, D. F. Dubois, G. A. Kyrala, D. S. Montgomery, H. A. Rose, H. X. Vu, R. G. Watt, B. H. Wilde, M. D. Wilke, W. M. Wood, B. H. Failor, R. K. Kirkwood, and B. J. Macgowan, Measurements of laser-plasma instability relevant to ignition hohraums, *Phys. Plasmas* **4**, 1849 (1997).
3. D. S. Montgomery, B. B. Afeyan, J. A. Cobble, J. C. Fernandez, M. D. Wilke, S. H. Glenzer, R. K. Kirkwood, B. J. Macgowan, J. D. Moody, E. L. Lindman, D. H. Munro, B. H. Wilde, H. A. Rose, D. F. Dubois, B. Bezzerides, and H. X. Vu, Evidence of plasma fluctuations and their effect on the growth of stimulated Brillouin and stimulated Raman scattering in laser plasmas, *Phys. Plasmas* **5**, 1973 (1998).
4. B. Bezzerides, D. F. Dubois, and H. A. Rose, Saturation of stimulated Raman Scattering by the excitation of strong Langmuir turbulence, *Phys. Rev. Lett.* **70**, 2569 (1993).
5. D. Russell, D. F. Dubois, and H. A. Rose, Nonlinear saturation of stimulated Raman scattering in laser hot spots, *Phys. Plasmas* **6**, 1294 (1999).
6. J. M. Dawson, Particle simulations of plasmas, *Rev. Mod. Phys.* **55**, 403 (1983).
7. H. X. Vu and J. U. Brackbill, CELEST1D: An implicit, fully-kinetic model for low-frequency, electromagnetic plasma simulation, *Comput. Phys. Commun.* **69**, 253 (1992).
8. J. U. Brackbill and D. W. Forslund, An implicit method for electromagnetic plasma simulation in two dimensions, *J. Comput. Phys.* **46**, 271 (1982).
9. D. W. Forslund and J. U. Brackbill, *Phys. Rev. Lett.* **48**, 1614 (1982).
10. J. U. Brackbill and D. W. Forslund, Simulation of low-frequency electromagnetic phenomena in plasmas, in *Computational Techiques: Multiple Time Scales*, edited by J. U. Brackbill and B. I. Cohen (Academic Press, Orlando, FL, 1985).
11. D. Dickman, R. L. Morse, and C. W. Nielson, Numerical simulation of axisymmetric, collisionless, finite-β plasma, *Phys. Fluids* **12**, 1708 (1969).
12. A. B. Langdon, Effects of the spatial grids in simulation plasmas, *J. Comput. Phys.* **6**, 247 (1970).
13. A. B. Langdon and B. F. Lasinski, Electromagnetic and relativistic plasma simulation models, *Methods Comput. Phys.* **16**, 327 (1976).
14. C. W. Nielson and H. R. Lewis, Particle-code model in nonradiative limits, *Methods Comput. Phys.* **16**, 367 (1976).
15. J. Busnardo-Neto, P. L. Pritchett, A. T. Lin, and J. M. Dawson, A self-consistent magnetostatic particle code for numerical simulation of plasmas, *J. Comput. Phys.* **23**, 300 (1977).
16. J. A. Byers, B. I. Cohen, W. C. Condit, and J. D. Hanson, Hybrid simulations of quasineutral phenomena in magnetized plasma, *J. Comput. Phys.* **27**, 363 (1978).
17. D. W. Hewett and C. W. Nielson, A multidimensional quasineutral plasma simulation model, *J. Comput. Phys.* **29**, 219 (1978).
18. D. W. Hewett, A global method for solving the electron-field equations in a zero-inertia electron-hybrid plasma simulation code, *J. Comput. Phys.* **38**, 378 (1980).
19. R. J. Mason, Implicit moment particle simulation of plasmas, *J. Comput. Phys.* **41**, 233 (1981).
20. J. Denavit, Time filtering particle simulations with $\omega_{pe}\Delta t \gg 1$, *J. Comput. Phys.* **42**, 337 (1981).
21. R. J. Mason, Hybrid and collisional implicit plasma simulation models, in *Computational Techiques: Multiple Time Scales*, edited by J. U. Brackbill and B. I. Cohen (Academic Press, Orlando, FL, 1985).
22. B. I. Cohen, Orbit averaging and subcycling in particle simulation of plasmas, in *Computational Techiques: Multiple Time Scales*, edited by J. U. Brackbill and B. I. Cohen (Academic Press, Orlando, FL, 1985).
23. A. B. Langdon and D. C. Barnes, Direct implicit plasma simulations, in *Computational Techiques: Multiple Time Scales*, edited by J. U. Brackbill and B. I. Cohen (Academic Press, Orlando, FL, 1985).
24. R. W. Hockney and J. W. Eastwood, *Computer Simulation Using Particles* (Adam Hilger, New York, 1988).

25. H. X. Vu, J. U. Brackbill, and D. Winske, Multiple switch-off slow shock solutions, *J. Geophys. Res.* **97**, 13839 (1992).
26. J. U. Brackbill and H. X. Vu, Electron kinetic effects in switch-off slow shocks, *Geophys. Res. Lett.* **20**, 2015 (1993).
27. D. W. Forslund, J. M. Kindel, and E. L. Lindman, Plasma simulation studies of stimulated scattering processes in laser-irradiated plasmas, *Phys. Fluids* **18**, 1017 (1975).
28. A. Ghizzo, T. Reveille, P. Bertrand, T. W. Johnston, J. Lebas, and M. Shouchri, An Eulerian Vlasov-Hilbert code for the numerical simulation of the interaction of high-frequency electromagnetic waves with plasmas, *J. Comput. Phys.* **118**, 356 (1995).
29. K. Estabrook, S. C. Wilks, W. L. Kruer, J. Denavit, D. E. Hinkle, D. Kalantar, A. B. Langdon, B. J. Macgowan, D. Montgomery, J. Moody, and E. A. Williams, Nonlinear theory and simulations of stimulated Brillouin backscatter in multi-ion plasmas, *Bull. Am. Phys.* **39**, 1733 (1994).
30. S. C. Wilks, W. L. Kruer, R. L. Berger, E. A. Williams, and J. Denavit, Studies of stimulated Brillouin scattering using a hybrid particle ion/fluid electron code, in *Proceedings, Twenty-Second Annual Anomalous Absorption Conference, Lake Placid, NY, July 1992.*
31. H. X. Vu, An adiabatic fluid electron particle-in-cell code for simulating ion-driven parametric instabilities, *J. Comput. Phys.* **124**, 417 (1996).
32. H. X. Vu, A massively parallel three-dimensional hybrid code for simulating ion-driven parametric instabilities, *J. Comput. Phys.* **144**, 257 (1998).
33. H. X. Vu, Three-dimensional particle-in-cell simulations of ion-driven parametric instabilities, *Phys. Plasmas* **4**, 1841 (1997).
34. K. Y. Sanbonmatsu, H. X. Vu, D. F. Dubois, and B. Bezzerides, New paradigm for the self-consistent modeling of wave-particle and wave-wave interactions in the saturation of electromagnetically driven parametric instabilities, *Phys. Rev. Lett.* **82**, 932 (1999).
35. H. A. Rose, Saturation of stimulated Brillouin scatter by self-consistent flow profile modification in laser hot spots, *Phys. Plasmas* **4**, 437 (1997).
36. D. W. Forslund, J. M. Kindel, and E. L. Lindman, Theory of stimulated scattering processes in laser-irradiated plasmas, *Phys. Fluids* **18**, 1002 (1975).
37. R. W. Hockney, Measurements of collision and heating times in a two-dimensional thermal computer plasma, *J. Comput. Phys.* **8**, 19 (1971).